2006

Measuring Optical Turbulence Parameters With A Three-aperture Receiver

David Wayne
University of Central Florida

MEASURING OPTICAL TURBULENCE PARAMETERS WITH A THREE-APERTURE RECEIVER

by

DAVID T. WAYNE
B.S.E.E. Grand Valley State University, 2004

A thesis submitted in partial fulfillment of the requirements
for the degree of Master of Science
in the Department of Electrical Engineering
in the College of Engineering and Computer Science
at the University of Central Florida
Orlando, Florida

Fall Term
2006

ABSTRACT

This thesis discusses methods to measure several atmospheric parameters related to turbulence. Techniques used by two different scintillometers based on weak turbulence theory are discussed along with a method to estimate the inner scale developed by Hill. The theory and minimization algorithm used to infer the atmospheric parameters are discussed. The main focus is on the analysis and collection of experimental data with a three-aperture receiver system. Intensity fluctuations from a CW laser source are collected over a 1km path with three different receiving apertures. The scintillation index is found for each receiving aperture and recently developed theory for all regimes of optical turbulence is used to infer three atmospheric parameters, C_n^2, l_0, and L_0. The transverse wind speed is also calculated from the experimental data using a cross-correlation technique. Parallel to the three-aperture data collection is a commercial scintillometer unit which reports C_n^2 and crosswind speed. There is also a weather station positioned at the receiver side which provides point measurements for temperature and wind speed.

The C_n^2 measurement obtained from the commercial scintillometer is used to infer l_0, L_0, and the scintillation index. Those values are then compared to the inferred atmospheric parameters from the experimental data. Hill's method is used as an estimate to l_0 based upon path-averaged wind speed and is compared to the inferred l_0 values. The optimal aperture sizes required for three-aperture data collection are presented. In closing, the technique for measuring crosswind speed is discussed along with the ideal aperture size and separation distance for data collection. Suggestions are offered for future experimentation.

ACKNOWLEDGMENTS

I would like to thank Dr. Ron Phillips and Dr. Larry Andrews for their knowledge, guidance, and time.

TABLE OF CONTENTS

LIST OF FIGURES

LIST OF TABLES

LIST OF ACRONYMS/SYMBOLS

$\langle \cdot \rangle$ ..... Ensemble Average

C_n^2 ..... Refractive index structure parameter

CW ..... Continuous Wave

DAC ..... Data Acquisition Card

FSO ..... Free Space Optical

IR ..... Infrared

ISTEF ..... Innovative Science and Technology Experimentation Facility

LED ..... Light Emitting Diode

l_0 ..... Inner scale of turbulence

L_0 ..... Outer scale of turbulence

NOAA ..... National Oceanic and Atmospheric Administration

PMT ..... Photomultiplier Tube

R_f ..... Fresnel zone

RMS ..... Root Mean Square

SNR ..... Signal to Noise Ratio

CHAPTER 1: INTRODUCTION

Ever since Maiman stimulated the emission of light from a ruby rod in 1960, many uses for the laser have come about. The laser was found to have many uses in physics, chemistry, and the communications industry. Optical frequencies allowed for higher bandwidth, faster data rates, and increased security. Optical communications started with optical fiber as the channel, but soon progressed to using the atmosphere as the channel; thus FSO was born. The atmosphere posed some obstacles before it could be used as a reliable communications channel.

At the short wavelengths of optical waves, problems arose that were not a concern with RF communication. Three of those problems were absorption, scattering, and turbulence. Absorption of optical waves results in attenuation, it occurs throughout the visible and IR spectrum. Absorption is a selective process and results from specific molecules in the atmosphere having an absorption band at an optical wavelength. Scattering occurs when a particle in the atmosphere is on the same order of magnitude of the optical wavelength.[1] The interaction of the particle and light wave causes an angular redistribution of a portion of the radiated wave. Optical turbulence is a result of fluctuations in the index of refraction along a propagation path. These fluctuations distort the phase front and vary the temporal intensity of an optical wave. The combination of these atmospheric effects on an optical system can cause phenomena such as beam spreading, image dancing, beam wander, and scintillation.[2]

Scintillation occurs when there is a temperature gradient, due to say hot asphalt surface with cool air above it. The scintillation is the steam appearing to be rising up from the asphalt surface.

Where the temperature gradient is highest, hot surface, the scintillation is most pronounced. As the temperature gradient decreases, higher above the hot surface, the effects of scintillation begin to decrease. The above description assumes frozen turbulence, no wind. When a wind velocity is considered, it causes the large cells to break up into turbulent cells called eddies. The theory used in this thesis classifies these eddies as either small scale or large scale. The small scale has a diffractive or spreading effect, while the large scale has a refractive or focusing effect on the optical wave.

Since the 1970's there have been studies on the effects of scintillation on a laser beam propagating through the atmosphere. Many methods have been developed to infer atmospheric parameters such as the refractive index structure parameter, C_n^2, and the inner scale of turbulence, l_0. These methods have been proven accurate in the presence of weak turbulence and over short path lengths.[7] Commercial instruments have been developed based upon 1970's theory and are currently the best available.[7] This research explores the theory and implementation of a new technique to infer four important atmospheric parameters, C_n^2, l_0, L_0, and crosswind speed, from the measured scintillation index at thee different sized apertures, where L_0 is the outer scale of turbulence. These parameters are necessary to characterize the effects of optical turbulence on a laser beam propagating through the atmosphere.

CHAPTER 2: BACKGROUND

This section reviews necessary mathematical concepts such as the structure function, spatial covariance function, and the cross-covariance. This section also defines the atmospheric parameters of interest; the index of refraction structure parameter, inner and outer scale of turbulence, Rytov variance, and the scintillation index. These concepts and definitions will be used throughout this report. The derivations and definitions in this chapter follow those found in *Laser Beam Propagation through Random Media 2nd Edition*.

Structure Function

The structure function is introduced when a random process can no longer be considered stationary. Some examples of this are wind velocity fluctuations and temperature fluctuations; they are not stationary because their means are constant only over a short period of time. To overcome this problem, the random process is considered to have *stationary increments*. Instead of working directly with the random process, the function $x(t + t_1) - x(t_1)$ is introduced. Such functions are considered to have a slow varying mean and can be easily described using structure functions.

In the study of stationary increments, a random process, $x(t)$, is written as the sum of the mean, $m(t)$, and a fluctuating part, $x_1(t)$, where $\langle x_1(t) \rangle = 0$,

$$x(t) = m(t) + x_1(t) \,. \tag{1}$$

Where $\langle \cdot \rangle$ denotes the ensemble average. The structure function associated with the random process *x(t)* is,

$$D_x(t_1, t_2) = \left\langle [x(t_1) - x(t_2)]^2 \right\rangle \tag{2}$$

$$= [m(t_1) - m(t_2)]^2 + \left\langle [x_1(t_1) - x_1(t_2)]^2 \right\rangle . \tag{3}$$

It is important to note that if the mean is "slowly varying" then the first term reduces to zero and the structure function is approximated by,

$$D_x(t_1, t_2) \cong \left\langle [x_1(t_1) - x_1(t_2)]^2 \right\rangle . \tag{4}$$

This concept can be easily extended into the spatial domain. The spatial equivalent to *stationary increments* is *locally homogeneous*. This allows a random field to be written in the spatial domain as

$$x(\mathbf{R}) = m(\mathbf{R}) + x_1(\mathbf{R}) \,, \tag{5}$$

where **R** a position vector in space. Applying the same concept used for a random process with *stationary increments*, the structure function for a locally homogeneous random field can be written as

$$D_x(\mathbf{R}_1, \mathbf{R}_2) = D_x(\mathbf{R}) = \left\langle \left[x(\mathbf{R}_1) - x(\mathbf{R}_1 + \mathbf{R}) \right]^2 \right\rangle . \tag{6}$$

Spatial Covariance Function

In the analysis of the covariance function in the spatial domain, the time dependent portion of the random field is suppressed. The mean of the random field, $x(\mathbf{R})$, is denoted by

$$\langle x(\mathbf{R}) \rangle = m(\mathbf{R}) . \tag{7}$$

The associated covariance function is defined by the ensemble average

$$B_x(\mathbf{R}_1, \mathbf{R}_2) = \left\langle \left[x(\mathbf{R}_1) - m(\mathbf{R}_1) \right] \left[x^*(\mathbf{R}_2 - m^*(\mathbf{R}_2)) \right] \right\rangle , \tag{8}$$

where * denotes the complex conjugate. The random field is considered statistically homogeneous if the moments of the covariance function are invariant under a spatial translation;

that is, the mean value of the random field is independent of spatial position, **R**, thus making the covariance function dependent on $\mathbf{R} = \mathbf{R}_2 - \mathbf{R}_1$. The covariance function can be rewritten as

$$B_x(\mathbf{R}) = \left\langle x(\mathbf{R}_1)x^*(\mathbf{R}_1 + \mathbf{R})\right\rangle - |m|^2, \tag{9}$$

where | | represents the absolute value. The random field is statistically isotropic if the random field exhibits invariance properties; that is the covariance function depends only in the scalar distance $R = |\mathbf{R}_2 - \mathbf{R}_1|$. Assuming both a statistically homogeneous and isotropic random field, the covariance function can be rewritten as

$$B_x(R) = \left\langle x(R_1)x^*(R_1 + R)\right\rangle - |m|^2. \tag{10}$$

Index of Refraction Structure Parameter, C_n^2

Physically, the refractive-index structure parameter, C_n^2, is a measure of the strength of the fluctuations in the refractive index. The index of refraction of a medium is important when propagating light through it. The atmosphere exhibits random fluctuations in refractive index as the temperature and wind speed change. At a point **R** in space and time *t*, the index of refraction can be mathematically expressed as

$$n(\mathbf{R},t) = n_0 + n_1(\mathbf{R},t), \tag{11}$$

where $n_0 = \langle n(\mathbf{R},t) \rangle \cong 1$ is the mean value of the index of refraction and $n_1(\mathbf{R},t)$ represents the random deviation of $n(\mathbf{R},t)$ from its mean value; thus, $\langle n_1(\mathbf{R},t) \rangle = 0$. Typically time variations of the refractive index are slow compared to the frequency of the optical wave; therefore the wave is assumed to be monochromatic. The expression in (11) can then be written as

$$n(\mathbf{R}) = 1 + n_1(\mathbf{R}), \tag{12}$$

where $n(\mathbf{R})$ has been normalized by its mean value n_0.

The index of refraction for the atmosphere can be written for visible and IR wavelengths as

$$n(\mathbf{R}) = 1 + 77.6 \times 10^{-6} \left(1 + 7.52 \times 10^{-3} \lambda^{-2}\right) \frac{P(\mathbf{R})}{T(\mathbf{R})}, \tag{13}$$

where λ, the optical wavelength, is expressed in μm, P(**R**) is the pressure in millibars at a point in space, and T(**R**) is the temperature in Kelvin at a point in space. It is noticed that the wavelength dependence for optical frequencies is very small; equation 13 can then be rewritten as

$$n(\mathbf{R}) \cong 1 + 79 \times 10^{-6} \frac{P(\mathbf{R})}{T(\mathbf{R})}. \tag{14}$$

Since pressure fluctuations are usually negligible, the index of refraction exhibits an indirect relation with the random temperature fluctuations. This simple approximation only holds in the visible and near-IR regime. Extending the wavelength into the far-IR introduces other issues such as humidity.

Since $\langle n_1(\mathbf{R}, t) \rangle = 0$, the spatial covariance of $n(\mathbf{R})$ can be expressed as

$$\mathbf{B}_n(\mathbf{R}_1, \mathbf{R}_2) = B_n(\mathbf{R}_1, \mathbf{R}_1 + \mathbf{R}) = \langle n_1(\mathbf{R}_1) n_1(\mathbf{R}_1 + \mathbf{R}) \rangle. \tag{15}$$

If the random field is both statistically homogeneous and isotropic, the spatial covariance function can be expressed in terms of a scalar distance $R = |\mathbf{R}_2 - \mathbf{R}_1|$. Assuming statistically homogeneous and isotropic turbulence, the related structure function exhibits asymptotic behavior

$$D_n(R) = \begin{cases} C_n^2 R^{2/3}, & l_0 << R << L_0 \\ C_n^2 l_0^{-4/3} R^2, & R << l_0 \end{cases}, \tag{16}$$

where C_n^2 is the index-of-refraction structure parameter, l_0 is the inner scale of turbulence, and L_0 is the outer scale of turbulence. The inner and outer scales of turbulence act as a lower and

upper bound, respectively, for the fluctuations of the refractive index. Behavior of C_n^2 at a point along the propagation path can be deduced from the temperature structure function obtained from point measurements of the mean-square temperature differences in two fine wire thermometers. With the use of equation 14,

$$C_n^2 = \left(79 \times 10^{-6} \frac{P}{T^2}\right)^2 C_T^2 . \tag{17}$$

Typical values for C_n^2 are between $10^{-16} m^{-2/3}$ for weak fluctuations and $10^{-12} m^{-2/3}$ for strong fluctuations. Figure 1 illustrates the behavior of C_n^2 throughout a typical day. The data was taken using a commercial scintillometer at the ISTEF laser range. When there is no sunshine, C_n^2 is low. As the sun begins to rise, C_n^2 increases until it reaches a maximum in the middle of the day. As the sun begins to set, C_n^2 decreases. An interesting trend to note on the plot is the dip in C_n^2 before and after sunrise. These two dips are called the quiescent periods. This drop in C_n^2 occurs due to the temperature gradient between the ground and atmosphere being minimal.

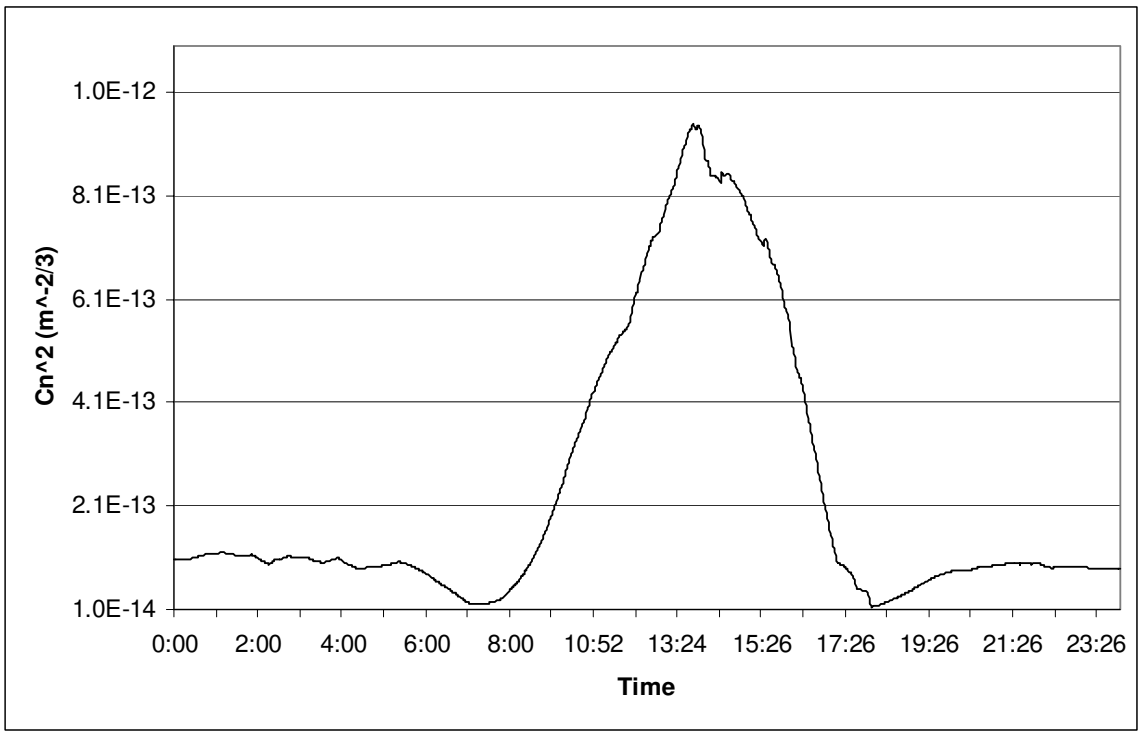

Figure 1: 24-hour C_n^2 profile.

Inner and Outer Scale, l_0 and L_0

A combination of temperature and wind speed variations cause unstable air masses, which break up into turbulent eddies of varying sizes. The maximum size, which is usually on the order of one to one hundred meters, is known as the outer scale L_0. Due to inertial forces, these eddies will continually break up until reaching a minimum size on the order of millimeters, known as the inner scale l_0. After these eddies reach this minimum size, their rotational energy turns into heat. The inertial sub-range is defined as the group of eddies which lie between the outer scale and the inner scale. The eddies attenuate and redirect the energy of a propagating laser beam

based on the relative size of the wave front in relation to l_0 and L_0.[2] Figure 2 illustrates the inertial sub-range and the formation of the inner scale from the outer scale.[2]

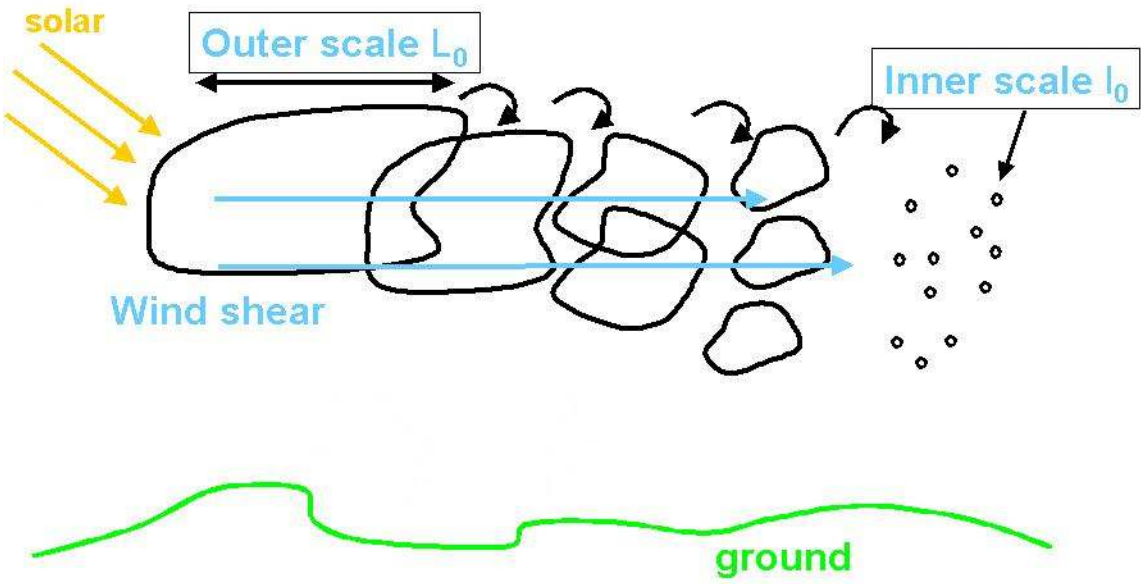

Figure 2: Outer scale breaking up into inner scale.

Rytov Variance

The Rytov variance is used when studying the propagation of plane or spherical waves in the Kolmogorov spectrum. The Kolmogorov spectrum represents the associated power spectral density for refractive-index fluctuations over the inertial sub-range.[3] It is defined as

$$\Phi_n(\kappa) = 0.033 C_n^2 \kappa^{-11/3}, \; 1/L_0 << \kappa << 1/l_0, \tag{18}$$

where κ represents the scalar spatial wave number. From this spectrum, the Rytov variance is

$$\sigma_1^2 = 1.23 C_n^2 k^{7/6} L^{11/6}. \tag{19}$$

The Rytov variance physically represents the irradiance fluctuations of an unbounded plane wave in weak optical turbulence, but is otherwise considered a measure of optical turbulence strength when extended to strong fluctuations.[3] Table 1 illustrates the use of the Rytov variance as a measure of the strength of optical turbulence.

Table 1: Turbulence strength in relation to Rytov variance.

Classification of Turbulence	Rytov Variance (σ_1^2)Value
Weak	< 1
Moderate	~ 1
Strong	$>> 1$
Saturation	$\rightarrow \infty$

Cross-Covariance

The cross-covariance function is a means of describing how similar two random signals are. To accomplish this, one random signal is held at a constant time and the other signal is shifted in time. This can be visualized as fixing one signal in time and "sliding" the other signal along the

time axis, similar to a convolution. The cross-covariance of two random processes, *x(t)* and *y(t)* at times t_1 and t_2 is defined as,

$$B_{xy}(t_1,t_2) = \left\langle \left[x(t_1) - \langle x(t_1) \rangle \right] \left[y(t_2) - \langle y(t_2) \rangle \right] \right\rangle = \left\langle x(t_1) y(t_2) \right\rangle - m_x(t_1) m_y(t_2) \quad (20)$$

Assuming a stationary random process, the cross-correlation function is simply the cross-covariance without the offset of the product of the means,

$$R_{xy}(t_1,t_2) = \left\langle x(t_1) y(t_2) \right\rangle \quad (21)$$

As opposed to the continuous case presented above, the cross-correlation can be computed in a discrete manner for two signals, *f(t)* and *g(t)* using the following formula,

$$R_{fg}(t_1,t_2) = \sum_j f^*(t_1) g(t_1 - t_j), \quad (22)$$

where t_j represents the number of samples to shift the signal.[5]

Scintillation Index

The scintillation index describes the fluctuations of the received irradiance after propagating through the atmosphere. It is calculated through the normalized variance of the irradiance fluctuations,

$$\sigma_I^2 = \frac{\langle I^2 \rangle}{\langle I \rangle^2} - 1 \quad , \tag{23}$$

where I represents the irradiance of the optical wave and $\langle I \rangle$ denotes the ensemble average.[2] Under weak turbulence conditions, $\sigma_I^2 < 1$, while in moderate to strong turbulence, $\sigma_I^2 \geq 1$. A plot of scintillation index versus the square root of the Rytov variance is shown in Figure 3. The plot was generated using commercially available laser beam propagation software manufactured by Ontar.

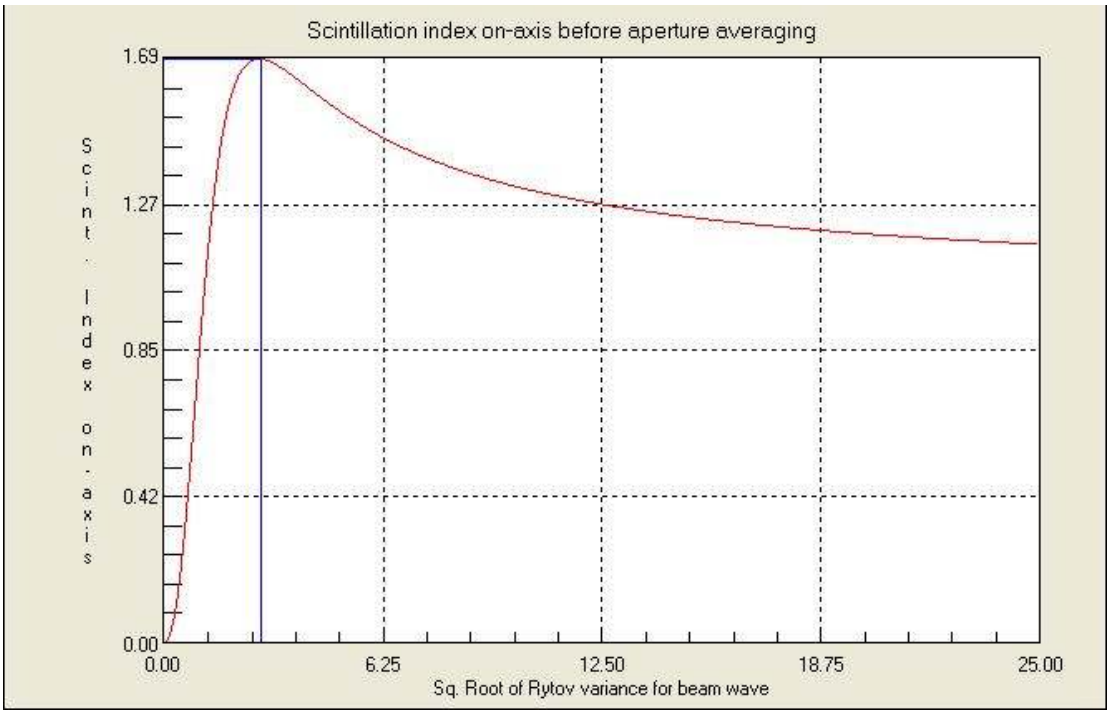

Figure 3: General plot of scintillation index.

This plot illustrates the peak fluctuations of irradiance occurring at a particular strength of optical turbulence. A reduction in the fluctuations occurs as the diameter of the receiving aperture is increased. The reduction is referred to as aperture averaging because the fast, more intense, fluctuations are averaged out. The scintillation index is also affected by both inner and outer scale. The inner scale effects are prominent in weak to moderate turbulence and cause an increase in scintillation index, while outer scale effects occur in strong turbulence and reduce the scintillation index. Figure 4 illustrates the effect of several different inner scale values on the scintillation index.[3] Figure 5 shows both the inner and outer scale contributions to the scintillation index.[3]

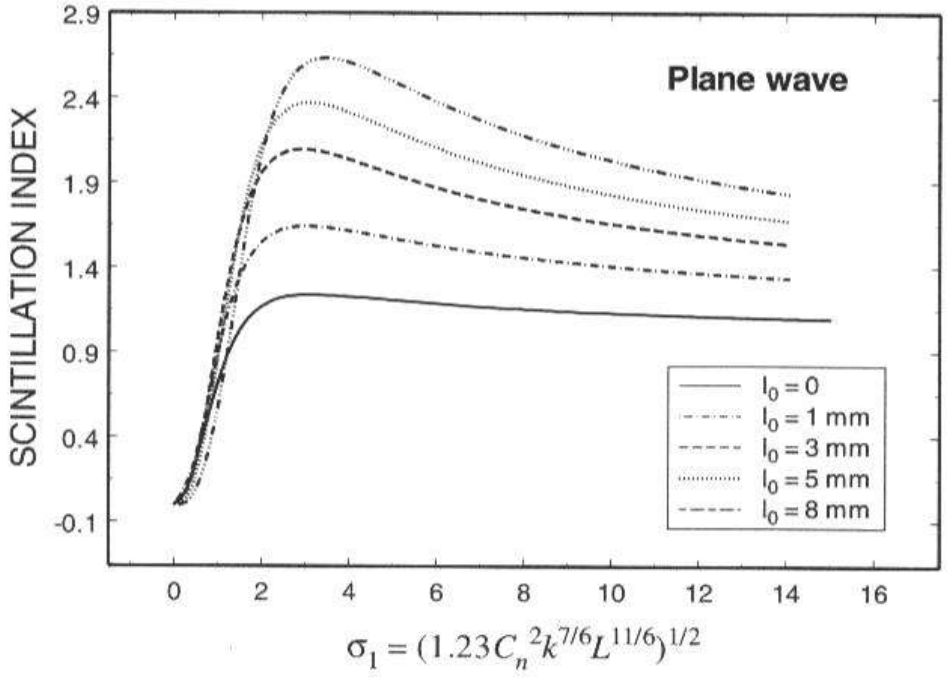

Figure 4: Effects of inner scale on the scintillation index.

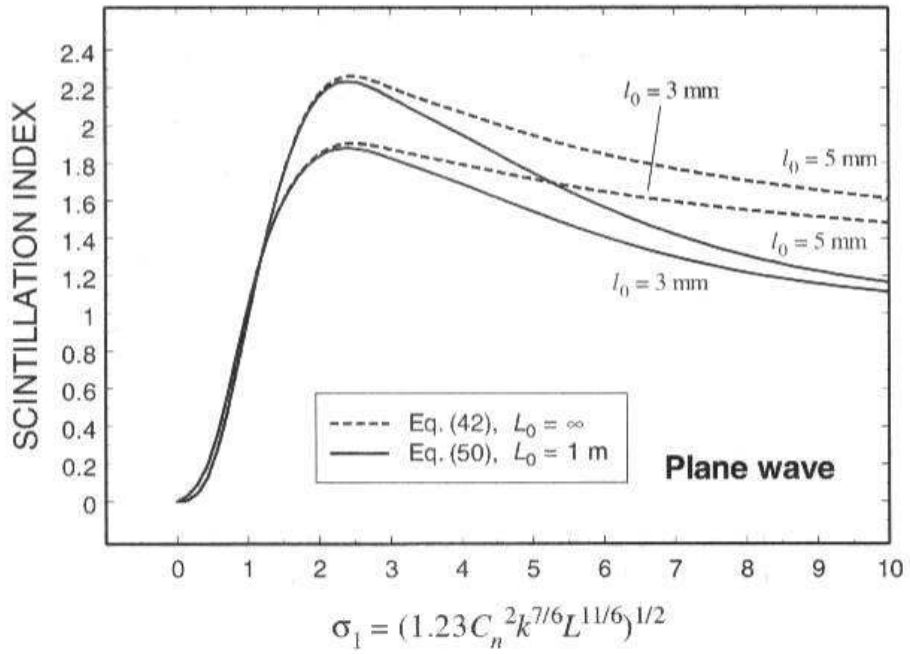

Figure 5: Effects of inner and outer scale on the scintillation index.

Theory

Under the Rytov approximation, the scintillation index can be expressed in terms of large scale and small scale log-irradiance variances, $\sigma_{\ln x}^2$ and $\sigma_{\ln y}^2$,

$$\sigma_I^2 = \exp\left(\sigma_{\ln I}^2\right) - 1 = \exp\left(\sigma_{\ln x}^2 + \sigma_{\ln y}^2\right) - 1 . \tag{24}$$

Upon properly filtering out the effects of intermediate scale sizes on the scintillation index, the Rytov approximation can be extended into the moderate to strong fluctuation regime. The irradiance of an optical wave can be thought of as a modulation of the small-scale (y) fluctuations by the large-scale (x) fluctuations.[8] The scintillation index at a point receiver is a function of three parameters, C_n^2, l_0, and L_0,

$$\sigma_I^2\left(l_0, L_0, C_n^2\right) = \exp\left(\sigma_{\ln x}^2\left(l_0, L_0, C_n^2\right) + \sigma_{\ln y}^2\left(l_0, C_n^2\right)\right) - 1 . \tag{25}$$

When theory is compared to experimental data, the averaging effects of a finite aperture must be accounted for. This results in the scintillation index also being a function of aperture diameter, D. Therefore, the theoretical expression for the scintillation index is,[8]

$$\sigma_I^2\left(l_0, L_0, C_n^2, D\right) = \exp\left(\sigma_{\ln x}^2\left(l_0, C_n^2, D\right) - \sigma_{\ln x}^2\left(l_0, L_0, C_n^2, D\right) + \sigma_{\ln y}^2\left(l_0, C_n^2, D\right)\right) - 1, \quad (26)$$

where $\sigma_{\ln x}^2$ and $\sigma_{\ln y}^2$ are defined in (APPENDIX A). Equation 27 shows the analytical approximation of the bump spectrum, published by Andrews[2], which was used in evaluating the scintillation index.

$$\Phi_n(\kappa) = 0.033 C_n^2 \kappa^{-11/3} \exp\left(\frac{-\kappa^2}{\kappa_l^2}\right)\left[1 + 1.80\left(\frac{\kappa}{\kappa_l}\right) - 0.25\left(\frac{\kappa}{\kappa_l}\right)^{7/6}\right] \quad (27)$$

Where $\kappa_l = \frac{3.3}{l_0}$.

CHAPTER 3: LITERATURE REVIEW

This chapter reviews research and equipment developed to measure optical turbulence parameters. First the theory behind a close range instrument for measuring C_n^2 and l_0 will be discussed. The technique used by a commercial scintillometer to measure C_n^2 and crosswind speed will be presented. A method to approximate l_0 from path-averaged wind speed and surface roughness will be presented. Finally, the minimization method used in this research to infer C_n^2, l_0, L_0 will be discussed.

Inner Scale, C_n^2 Instrument

In 1990, G.R. Ochs, J.K. Holler, and J.J. Wilson of NOAA built an inner scale meter. The instrument consisted of two scintillometer subsystems that together were able to resolve both l_0 and C_n^2. The method used to measure the scintillation was a modification of Livingston's work in 1972, using one transmitter and two receivers to make measurements. The NOAA inner scale meter used two independent transmitters and two independent receivers over a 150m path length. A subsystem sensitive to only C_n^2 was created using a large aperture for one of the receivers and an appropriate weighting function. An effective point aperture was used for the other receiver yielding a subsystem sensitive to both l_0 and C_n^2. The use of two different wavelengths for the two subsystems allowed both the smaller and larger spatial wavelengths to be measured. The

result was an instrument able to measure path averaged scale sizes throughout the entire inertial sub-range over a 150m path.[6]

Hill's model[6] was used in the calculations of l_0 and C_n^2. Hill's spectrum for a spherical wave is

$$\sigma_{\ln I}^2 = 0.5 C_n^2 k^{7/6} L^{11/6} f(l_0), \tag{28}$$

where $f(l_0)$ is the functional dependence on the bump spectrum. Figure 6 shows a normalized plot[6] of Hill's spectrum versus R_f/l_0, where R_f is defined in Equation 29,

$$R_f = \sqrt{\lambda L}\,. \tag{29}$$

The path distance and wavelength have been fixed at 150m and 0.6328μm respectively.

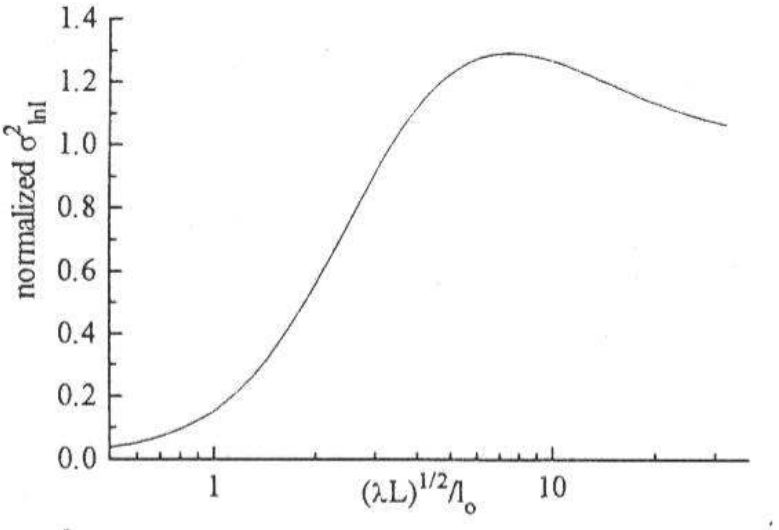

Figure 6: Normalized variance of log intensity, L = 150m, λ = 0.6328μm.

It was discovered that the diameter of the aperture, D, could be set so the variances would be independent of the wavelength. Setting the ratio, D/R_f, as small as 2.1 was sufficient enough to become wavelength independent. This discovery led to the concept of two receiving apertures, one large enough to be independent of wavelength and the other small enough to be sensitive to l_0, assuming $R_f / l_0 \approx 1$. The effect of l_0 on the scintillometer was considered by looking at the ratio[6]

$$\frac{\left(\sigma^2_{\ln I}\right)_1 D_1^{7/3}}{\left(\sigma^2_{\ln I}\right)_2 D_2^{7/3}}, \qquad (30)$$

where subscripts 1 and 2 denote the small and large apertures respectively. Equation 30 shows a relationship dependent on l_0, but independent of C_n^2. The ratio could then be used to generate a

plot similar to Figure 7, where a value of R_f / l_0 could be found, and therefore a value for l_0.[6] However, the value for l_0 was only an estimate and further correction would be needed to obtain an accurate inner scale value.

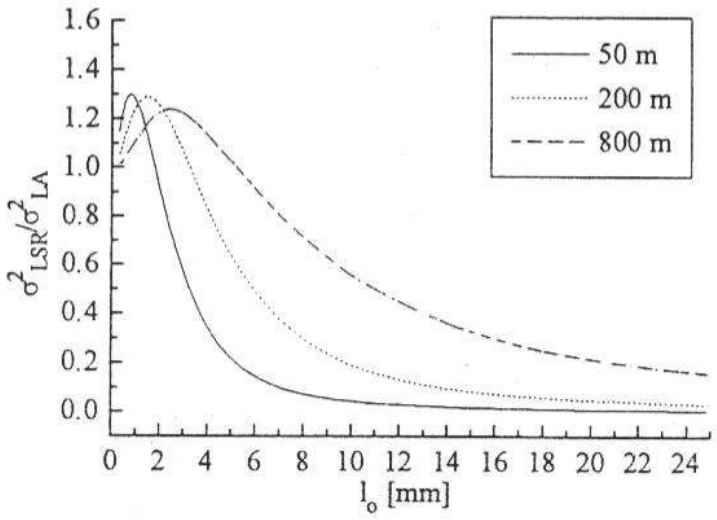

Figure 7: Plots of variance ratios vs. inner scale for several path lengths.

The large aperture scintillometer subsystem transmitted an incoherent modulated infrared LED transmitter. The 0.940μm LED was placed at the focus of a 4.4cm diameter lens, diverging the beam to ~10mrad. The LED was modulated to a 7kHz square wave and operated at a minimum of 100mW. At the receive side; the beam was focused with a 4.4cm diameter lens onto a photodiode. The received signal was passed through a bandpass gelatin filter with cutoffs at 0.880μm and 1.1μm. The signal was then processed to output a logarithmically scaled value of the received log-intensity.

The point aperture scintillometer subsystem transmitted a coherent light beam between the transmitter and the receiver. The receiving aperture was considered a point because its diameter was small compared to the speckle size, a result of optical turbulence. The transmitter was a CW 0.6328μm HeNe laser with a minimum power of 10mW. A lens was used to further diverge the beam to ~3mrad, thus producing a spherical wave at the receiver. A 1mm aperture coupled with a 1nm wavelength bandpass filter was used at the receiver. The signal was then processed to give an output of a logarithmically scaled value of the received log-intensity.

Based on the wavelengths and aperture sizes above, the calculations of l_0 and C_n^2 were only valid for a range of path lengths. The optimal operating path length for the inner scale meter was 150m. If the path were lengthened, the Fresnel zone would increase to values larger than the inner scale and the log-intensity fluctuations at the receiver would become less sensitive to l_0. This would create a limit on the lower bound value of inner scale that could be measured. For the upper bound, when the path length was significantly shorter than the Fresnel zone l_0 would become double valued. Figure 7 shows the log-intensity from the laser divided by the log-intensity from the large aperture versus l_0. The insensitivity to l_0 as the path length increases and the double values of l_0 as the path length decreases are easily understood from the plot in Figure 7.

Values were calculated for l_0 and C_n^2 through the use of a software program. The program used the logarithmically scaled outputs from the large aperture and point aperture scintillometer subsystems to define a ratio of the received intensity variances. The software checked for saturation of the signals and created corrected values for the path averaged l_0 and C_n^2 based upon

a look-up table. To make known double values of l_0 and values of l_0 below the limits of the look-up table, the software also created an error code.

The NOAA inner scale meter was not a practical instrument for measuring atmospheric parameters. It was based upon weak fluctuation theory, which breaks down as atmospheric turbulence increases along the measurement path. The instrument was optimized for a 150m path and would not work over longer distances with moderate to strong turbulence. Similarly, the instrument would not reliably measure the inner scale over a shorter path with moderate to strong turbulence. The instrument did not have the capability to measure wind speed or L_0, a critical parameter in moderate to strong turbulence.

Crosswind, C_n^2 Instrument

A German company named Scintec manufactures a series of instruments with the ability to measure crosswind speed and C_n^2 over path lengths up to 10km. Three models are offered, one able to measure only C_n^2 up to a distance of 5km(BLS450), another able to measure C_n^2 and crosswind speed up to a distance of 5km(BLS900), and another able to measure C_n^2 and crosswind speed up to a distance of 10km(BLS2000). The theory used to calculate C_n^2 in all the instruments is based upon weak scintillation. The assumption of weak turbulence can be made due to the structure of the scintillometer system. The transmitter and receiver aperture sizes are chosen so the system is relatively insensitive to saturation, roughly an order of magnitude larger

than l_0 and an order of magnitude smaller than L_0. The instrument corrects for saturation effects in strong turbulence by implementing a look-up table. Absorption fluctuations are also taken into account by the scintillometer, however only when $\sigma_I << 1$. The instrument also calculates Fried's parameter from C_n^2 and predicts the crosswind speed using the time-lagged cross-covariance function.

The BLS900 is the model of interest, as it was the model used to conduct experimentation. The BLS900 has two transmitters and one receiver. The two transmitting disks consist of 924 LEDs, 888 of which have a wavelength of 880nm. Figure 8 shows a dimensioned sketch, in millimeters, of the BLS900 transmitter.[7]

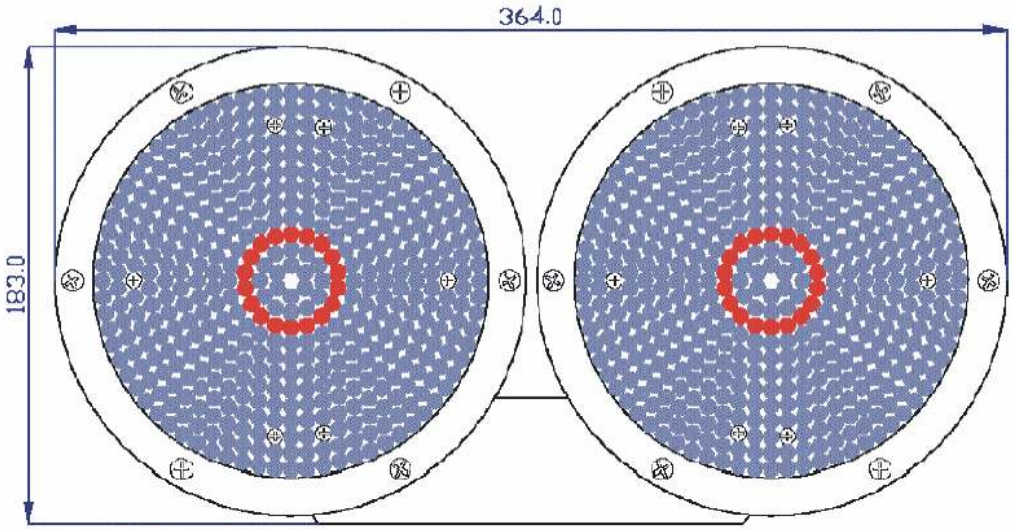

Figure 8: BLS900 scintillometer transmitter.

The disks are 0.15m in diameter, the large aperture size allows for homogeneous emission due to the many radiation sources. The inner rings of LEDs are a visible wavelength and used to tell

the operator the pulse frequency of the transmitter. Disks 1 and 2 have different modulation frequencies, 1,750Hz and 2,000Hz, respectively. The modulation reduces the background effects and allows the two signals to be separated by a single detector. The LEDs are operated at a pulsed rate. This allows for minimal power consumption at a low pulse rate (1Hz), or maximum accuracy at a high pulse rate (125Hz). The high pulse rate must be used to get a crosswind speed calculation. Inside the receiver resides two photodiodes, each of a different active area. The received radiation is collimated by a 145mm lens, which then irradiates the photodiodes. Figure 9 shows a dimensioned drawing, in millimeters, of the BLS900 receiver on mounting hardware.[7]

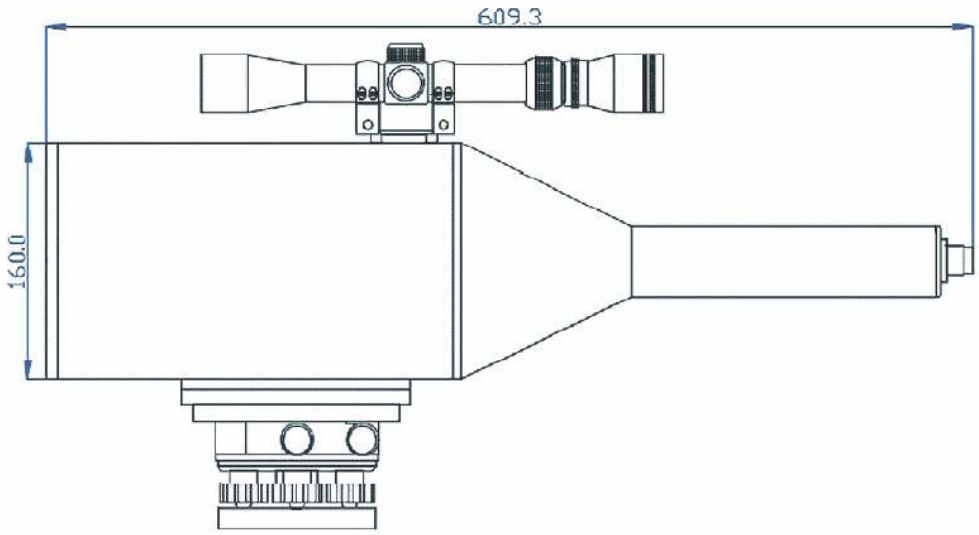

Figure 9: BLS900 scintillometer receiver.

One photodiode is used to sense the turbulence-induced fluctuations, while the other is strictly for alignment. The fluctuations received by the photodiode are processed with a signal-processing unit made by Scintec, the calculation results are then sent to a PC running Scintec's BLSRun software.

The three-dimensional spectrum used by the Scintec scintillometer is given by[7]

$$\Phi_n(\kappa) = 0.033 C_n^2 \kappa^{-11/3} f(\kappa\lambda_0) F(\kappa L_0), \tag{31}$$

where $f(\kappa\lambda_0)$ and $F(\kappa L_0)$ represent the effects of l_0 and L_0, respectively. The inner scale effects approach unity as $\kappa << 1/l_0$ and the outer scale effects approach unity as $\kappa >> 1/L_0$. Since the inner scale is typically on the order of millimeters and the outer scale is typically on the order of meters, the diameters chosen for the size of the radiating disks are not affected by the inner or outer scale. Also, by having the disks much larger than the Fresnel zone, the wavelength dependence is also eliminated. These assumptions are used to create a scintillometer independent of inner, outer scale, and wavelength.

The transverse wind speed, *u*, is derived from the time-lagged cross-covariance function, shown in equation 32,[7]

$$B_{12}(t) = 4\pi k^2 \int_0^\infty d\kappa \Phi_n(\kappa) \int_0^R dx \sin^2\left(\frac{k^2 x(R-x)}{2kR}\right)$$
$$J_0\left(\kappa(S_t - ut)\left(1 - \frac{x}{R}\right)\right)\left[2\frac{J_1\left(\frac{\kappa D_r x}{2R}\right)}{\frac{\kappa D_r x}{2R}}\right]^2\left[2\frac{J_1\left(\frac{\kappa D_t (R-x)}{2R}\right)}{\frac{\kappa D_t (R-x)}{2R}}\right]^2, \tag{32}$$

where x is the length coordinate along the propagation path, R is the propagation path length, D_r, and D_t are the receiver and transmitter diameters, respectively. The two $J_1(...)$ Bessel function terms account for aperture averaging at the receiver and transmitter. The time t of interest occurs when the cross-covariance function reaches its maximum value. A negative time would correspond to a change in wind direction.

The commercially available scintillometers from Scintec are commonly used in industry to measure some atmospheric parameters. The instruments are based on 1970's aperture averaging theory and do not take into account the effects of inner and outer scale. The instruments are capable of operating over various distances, but do not give reliable results over long, turbulent propagation paths.

Inferring Inner Scale from Wind Speed and Surface Roughness

In 1983 Hill proposed a method of estimating l_0 from the path averaged wind speed, surface roughness over which the laser beam propagates, and the height of the propagation path. The inner scale of turbulence is defined as,[4]

$$l_0 = 5.8\left(\frac{D^3}{\varepsilon}\right)^{1/4}, \tag{33}$$

where D is the diffusivity and ε is the dissipation rate. In the open atmosphere, $D = 0.22$ cm^2/s, yielding,[4]

$$l_0 = \frac{1.863\left[cm^{3/2}s^{-3/4}\right]}{\varepsilon^{1/4}}\left[cm\right]. \tag{34}$$

The dissipation rate, ε, can be related to the wind speed and surface roughness,

$$\varepsilon = \frac{0.16}{h}\left[\frac{\bar{u}}{\ln(h/h_r)}\right]^3 \left[cm^2/s^3\right], \tag{35}$$

where $\bar{u}$ is the path average wind speed in cm/s, h is the height above the ground in cm, and h_r is the surface roughness factor in cm. Substituting yields the complete equation for inner scale,

$$l_0 = 2.946\left[cm^{3/2}s^{-3/4}\right]h^{1/4}\left[\frac{\ln(h/h_r)}{\bar{u}}\right]^{3/4}\left[cm\right]. \tag{36}$$

For this experiment, the path height was 200cm and the surface roughness was estimated by the average grass height on the ISTEF range to be 5cm. These values were substituted into equation 36 and then the equation was rewritten using dimensional analysis to accept wind speed in m/s and output inner scale in mm.

$$l_0 = \frac{9.325}{\left(\bar{u}\right)^{3/4}} \left[mm\right], \tag{37}$$

where $\bar{u}$ is the path-averaged wind speed in m/s.

Inferring Inner Scale, Outer Scale, and C_n^2 from Three Apertures

Three parameters of optical turbulence, C_n^2, l_0, and L_0, can be calculated using the theory developed by Andrews et. al. To do this, the three parameters are inferred from experimentally measured scintillation indices of three different aperture sized receivers. A custom Mathematica program developed by Frida Stromqvist Vetelino[8,9], implements a minimization technique comparing theory to experimentation and calculates the parameters.

The custom Mathematica program required divergence, beam size, and wavelength of the transmitting laser, along with path length, receiving aperture sizes, and measured scintillation indices as inputs. The result was a system of three nonlinear equations with three unknowns,[8]

$$\sigma_I^2\left(l_0, L_0, C_n^2, D_j\right) = \sigma_{I,\exp}^2\left(D_j\right), \quad j = 1,2,3, \tag{38}$$

where the subscript *j* denotes different aperture sizes. Due to the complexity of the nonlinear equations, a numerical technique was used to solve for the unknowns. Instead of solving the three equations directly, a minimization problem was setup,

$$f\left(l_0, L_{0,} C_n^2\right) = \sum_{j=1}^{3} \left[\left|\sigma_I^2\left(l_0, L_0, C_n^2, D_j\right) - \sigma_{I,\exp}^2\left(D_j\right)\right|\right]^p \quad . \tag{39}$$

The downhill Simplex method was used to find the values of C_n^2, l_0, and L_0 that minimized the function in equation (39).[8]

CHAPTER 4: EXPERIMENTATION

Laboratory Setup

The experiments were performed at the ISTEF laser range in Cape Canaveral, Florida. The range was 1km long and approximately 4m wide. There was 1-2m high vegetation surrounding the length of the range. The propagation path was trimmed grass kept at approximately 5cm tall. Mobile laser propagation laboratories were placed at both ends of the range to provide a clean and dry environment to operate equipment. Both mobile laboratories were outfitted with an isolated 122cmx244cm optical bench, 5kVA uninterruptible power supply, safety glasses, laser curtain, air conditioner, and a window to propagate through. The transmitting laboratory was at the north end of the range, while the receiving laboratory was located at the south end. Figure 10 shows the setup of the laboratories on the ISTEF laser range.

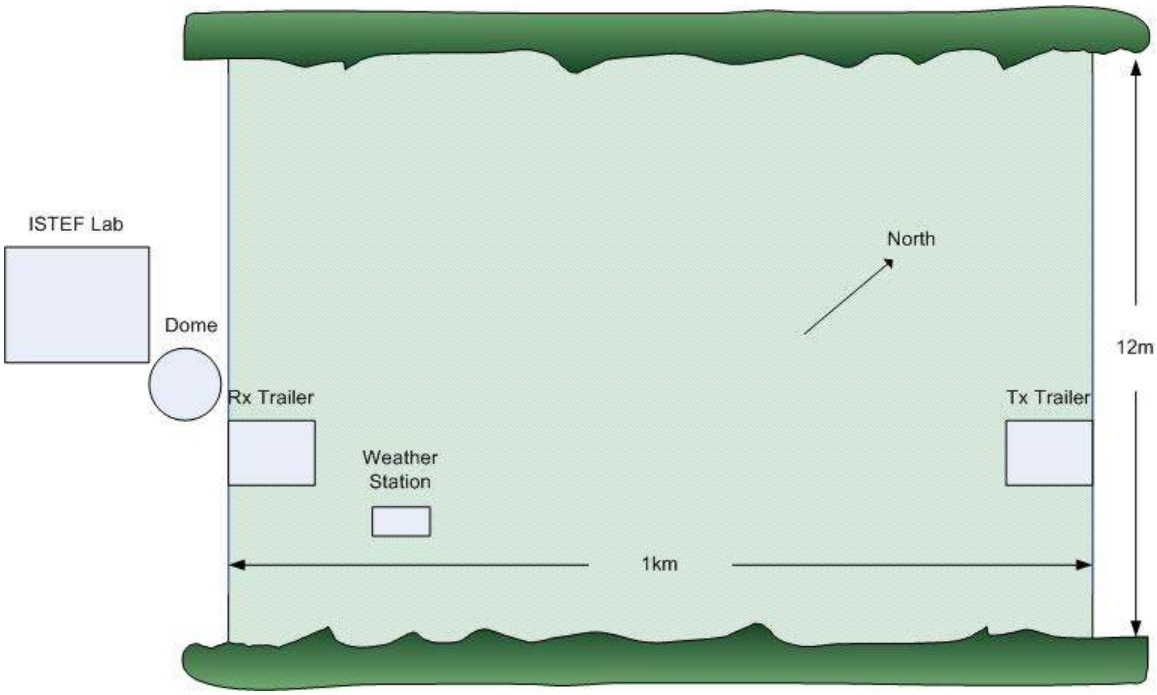

Figure 10: ISTEF range showing layout of experimental setup.

The transmitting laboratory was outfitted with a 150mW, 532nm, continuous wave, solid-state laser manufactured by Lightwave. It had a beam diameter of 0.42mm and a full-angle divergence of 1.6mrad. This laser was chosen due to availability, power output, and wavelength. A laser with enough power was needed to propagate 1km through atmospheric turbulence. Also, it was desired to use a laser in the 500nm region for ease of alignment and to satisfy the spectral response of the receivers. Besides a pair of 5cm mirrors configured in a figure eight for alignment, the laser passed through no optical components. A 220V electrical plug inside the ISTEF dome was used to power the receive trailer.

The transmitter of the BLS900 was also in the transmitting laboratory. The BLS900 used an array of eye-safe 880nm LEDs to transmit along the propagation path. The BLS900 transmitter

had no affect on the laser receivers because of filtering at the laser receivers. A 20kVA diesel generator powered the transmitting laboratory.

Inside the receiving laboratory were the three laser receivers and the receiver of the BLS900 scintillometer. Three Hamamatsu R1387 PMTs were used as the laser receivers. These were chosen because of availability, spectral response, and adjustable gain. The tubes were responsive over the range of 300 to 850nm and offered a maximum gain of approximately 10^6. Figure 11 illustrates the case used to mount the PMTs. The case was shielded from both electric and magnetic radiation, provided an environment with minimal stray light, and had a shutter to expose the face of the PMT. A single aperture was mounted inside the PMT case and within 1cm of the PMT face. The apertures were made from rubber coated cardboard discs. Cardboard was chosen for its availability, cost, and ease of machining. Mounting plates were manufactured to facilitate attaching sunshields in front of the shutter. The sunshields consisted of 2.54cm diameter anodized aluminum tubes lined with black flocking paper. The flocking paper eliminated any internal reflections inside the sunshields. At the rear of the sunshield for each PMT case were a series of filters. Each receiver had a 3nm bandwidth, 532nm laser line filter and a neutral density filter. Filtering was necessary to reduce the background light from the sun and increase the SNR. The neutral density filters were selected so the background was above the shot noise of the electrical log conversion circuit. The table below lists the neutral density filter values used for the different size apertures.

Table 2: Neutral density filter values used to increase SNR.

Aperture Size(mm)	Optical Density of Filter
1.0	1.5
6.0	3.0
25.4	4.0

Scintillation Index Data Collection

Each laser receiver was independently mounted on a tip-tilt stage to aid in alignment. Keithly high voltage power supplies were used to bias the cathode of each PMT with 500V. This voltage was chosen so the PMT would operate at a gain of 6,000. Although the gain of the PMT could be set as high as 10^6, the SNR would get compromised past a gain of 10^4. Connected to the Anode of the PMT was an electrical circuit that converted the negative current output of the PMT to a log-scaled voltage. An ADL5315 current mirror was used to convert the negative current generated by the PMT to a 1:1 positive current. The positive current from the mirror was input into an AD8304 logarithmic converter. The log converter compressed the dynamic range of the input current to a voltage output ranging from 0 to 1.6V. A four channel National Instruments data acquisition card was used to record the voltages to a computer running Labview at a rate of 1,000 samples every second. The data was collected over 7-minute data runs. The current mirror and the logarithmic converter were chosen because their dynamic range was larger than that of the PMT and the chips were already integrated into a circuit board. The DAC was chosen because of the number of channels, the high sampling rate, ease of integration with

Labview, and USB connectivity to a PC. Figure 11 shows the block diagram of a single laser receiver and the electronics described above. Figure 12 shows a dimensioned photo of the three PMTs setup in the mobile laboratory. Figure 13 shows the location of the BLS900 receiver relative to the PMT apertures.

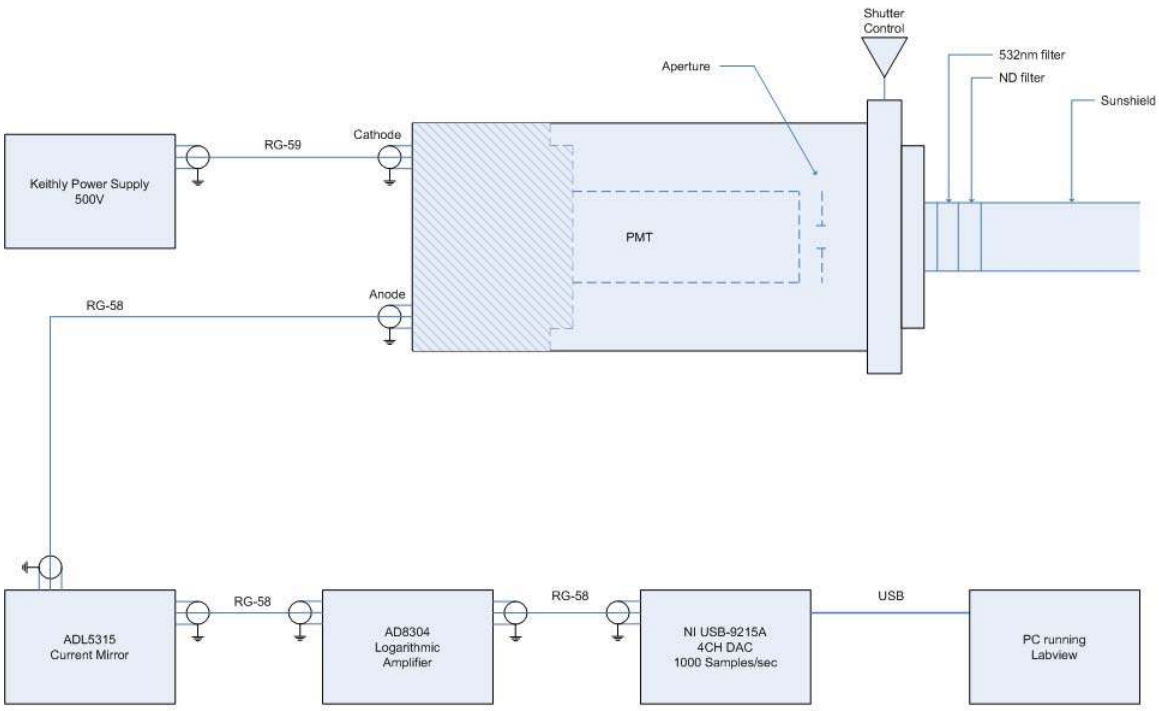

Figure 11: Block diagram of PMT receiver.

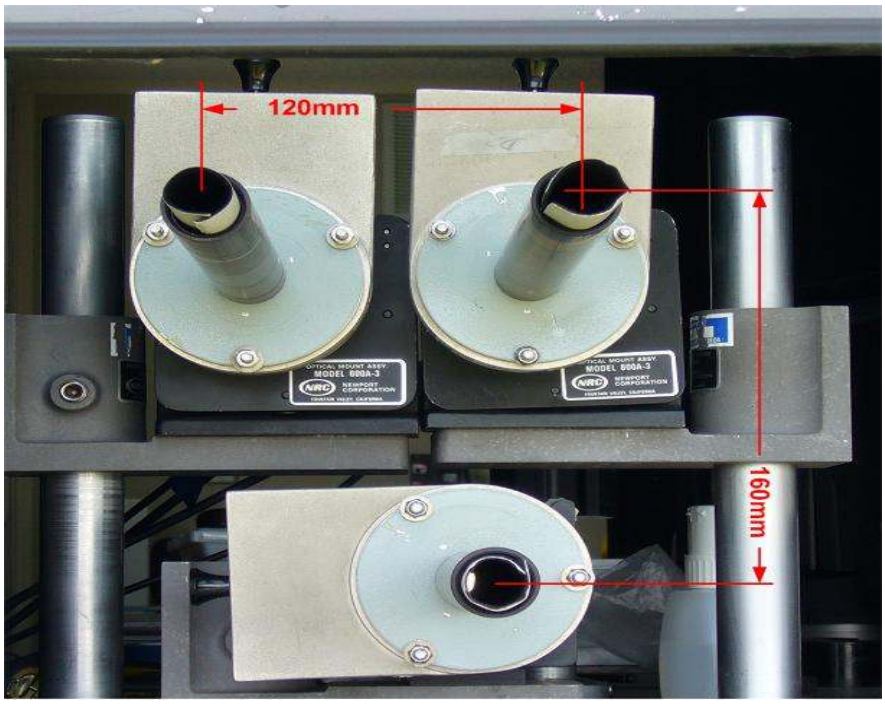

Figure 12: PMT receivers and commercial scintillometer receiver in use.

Figure 13: BLS900 receiver above PMT apertures.

Crosswind Speed Data Collection

Data were collected with the same hardware and software used in collecting the scintillation index data. In order to calculate crosswind speed, the experimental setup was altered. Two PMTs with apertures of the same diameter were setup at the same height on the optical bench. Figure 14 shows the configuration of the PMTs for data collection.

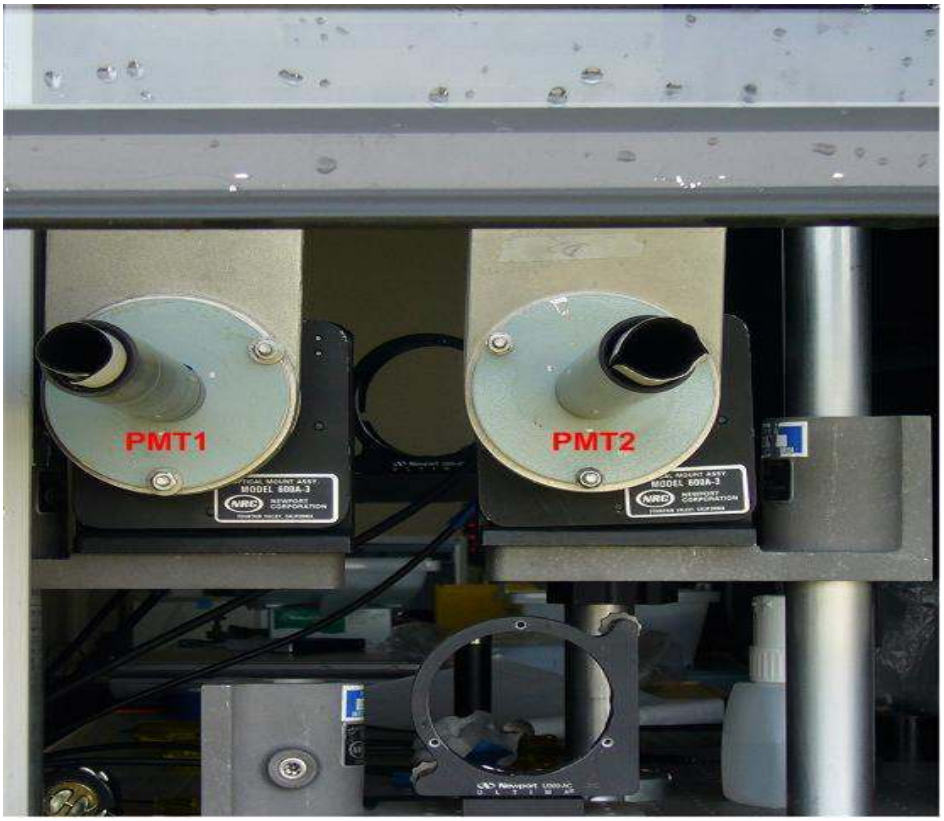

Figure 14: PMT configuration for crosswind speed data collection.

The received intensities from the two apertures were recorded with the DAC over 7-minute data runs. Two variables were used in this portion of data collection; the separation distance between the two receivers and the aperture size. Two aperture sizes, 25.4mm and 1mm, were used. A

larger aperture size was not used due to the limitation of the active area of the PMT. Data was collected at a minimum separation of 70mm and a maximum separation of 178mm. The range of separation was limited by the size of the PMT enclosures and available space on the optical table. When data were collected, the aperture sizes of the two receivers were the same size, unlike the scintillation index data collection.

CHAPTER 5: RESULTS

In all calculations, the data were first converted from a logarithmic to a linear format. Once in linear format, the scintillation index and cross-correlation were computed. Through the measured scintillation indices, the three optimal aperture sizes were found. Values for the scintillation indices from the three receiving apertures were entered into the custom Mathematica program and solutions for C_n^2, l_0, and L_0 were found. A custom Matlab program was used to compute the cross-correlation and determine the crosswind speed. The results are discussed.

Scintillation Index

Aperture Sizes

To begin processing the data, each data point needed to be converted from logarithmic to linear. The AD8304 logarithmic converter scaled each data point to 10mV/dB (200mV/decade). Equation (40) shows the conversion used to convert each data point to a linear format.

$$V_{Lin} = 100 \times 10^{-12} \left(10^{\frac{V_{Log}}{0.2}} \right) \tag{40}$$

The scintillation index was computed according to equation (23). The background was assumed to be constant throughout the 7-minute data run. Table 3 shows the average background measurement before and after a 7-minute data run. The values have been scaled by 10^{-7} for clarity.

Table 3: Average background intensity measurements from the three-apertures.

Aperture Size	Background Before Data Run	Background After Data Run
Small	0.775	0.914
Middle	0.567	0.708
Large	0.0483	0.0568

Under the assumption of a constant background, only a single one-minute background measurement was taken before the data run. In order to determine whether the average background needed to be subtracted from each measurement, the SNR was computed. The SNR was found to be at least 17dB for each data run; corresponding to a 3.5% change in scintillation index between values with the background subtracted and those without the background subtracted. The minor difference resulting from background subtraction stayed within the accuracy of the Mathematica program defined from experiments in February 2005.[8] Therefore the scintillation indices presented do not incorporate background subtraction.

In order to get converging solutions for C_n^2, l_0, and L_0 from the Mathematica program, the scintillation indices from the three apertures needed to be equally separated. Equal spacing compensated for the convergence at the tails of the scintillation index curves. To change the

difference between the scintillation indices, the aperture sizes needed to be adjusted. The largest aperture was selected based upon the Fresnel zone. Using equation (29), R_f equated to 23.1mm. The largest aperture needed to be at least the size of the Fresnel zone. The largest aperture available was 25.4mm; this fixed the upper limit of the three apertures. The smallest aperture was chosen based upon the speckle size of the received beam. The speckle size refers to the average size of the individual bright spots after a laser beam has been broken up, or speckled, due to atmospheric turbulence. Figure 15 illustrates the speckling of a beam after passing through turbulence.

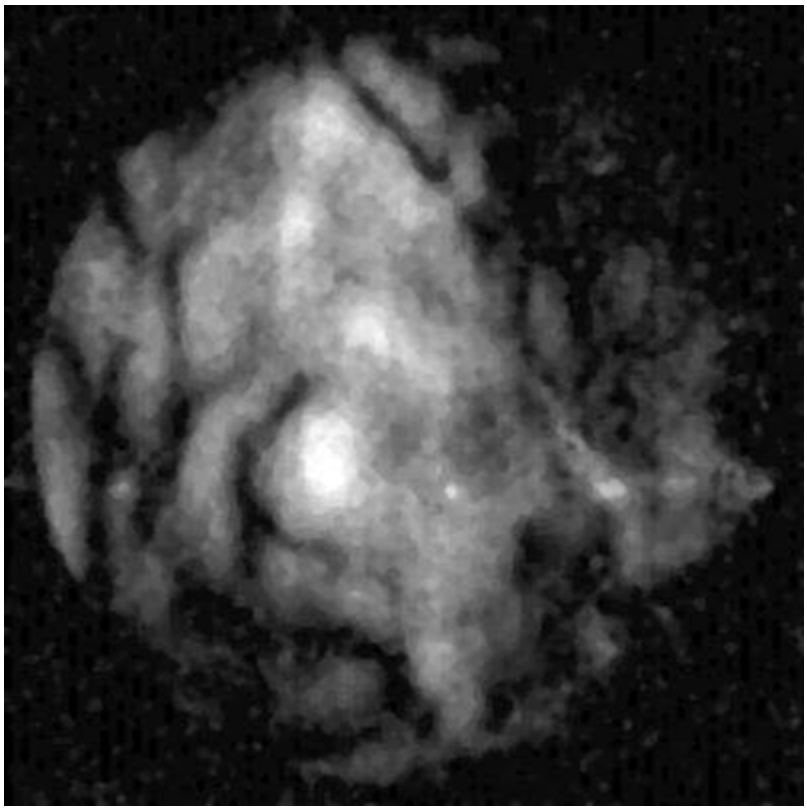

Figure 15: Laser beam breaking up after passing through turbulence.

The expression used to calculate the speckle size is given by,[2]

$$\rho_0 = \left(.55 C_n^2 \left(\frac{2\pi}{\lambda} \right)^2 L \right)^{-3/5} . \qquad (41)$$

The wavelength, λ, and the path length, L, were fixed at 532nm and 1,000m, respectively. A value of $C_n^2 = 7 \times 10^{-13}\, m^{-2/3}$ was chosen to represent a typical turbulent day at the ISTEF range. The above values were substituted into equation (41), yielding a speckle size of 1.4mm. The smallest aperture was then chosen as 1mm. Since the large and small aperture sizes were fixed, the middle-sized aperture was varied until equal separation between the scintillation indices was achieved. An aperture of 10mm was used as a starting point for the middle aperture. The aperture was then reduced to 6mm, which equally separated the scintillation indices of each receiving aperture. Figure 16 shows the scintillation indices calculated from the aperture sizes of 25.4mm, 10mm, and 1mm, while Figure 17 Shows the scintillation indices calculated from the aperture sizes of 25.4mm, 6mm, and 1mm.

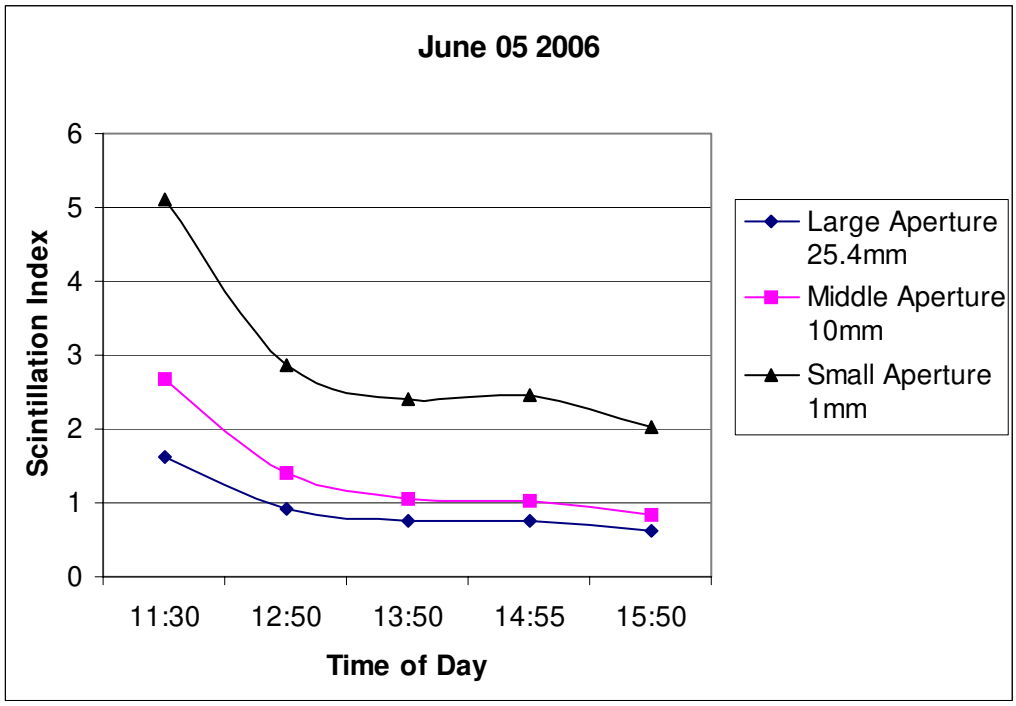

Figure 16: Scintillation indices using initial guess of three-aperture sizes.

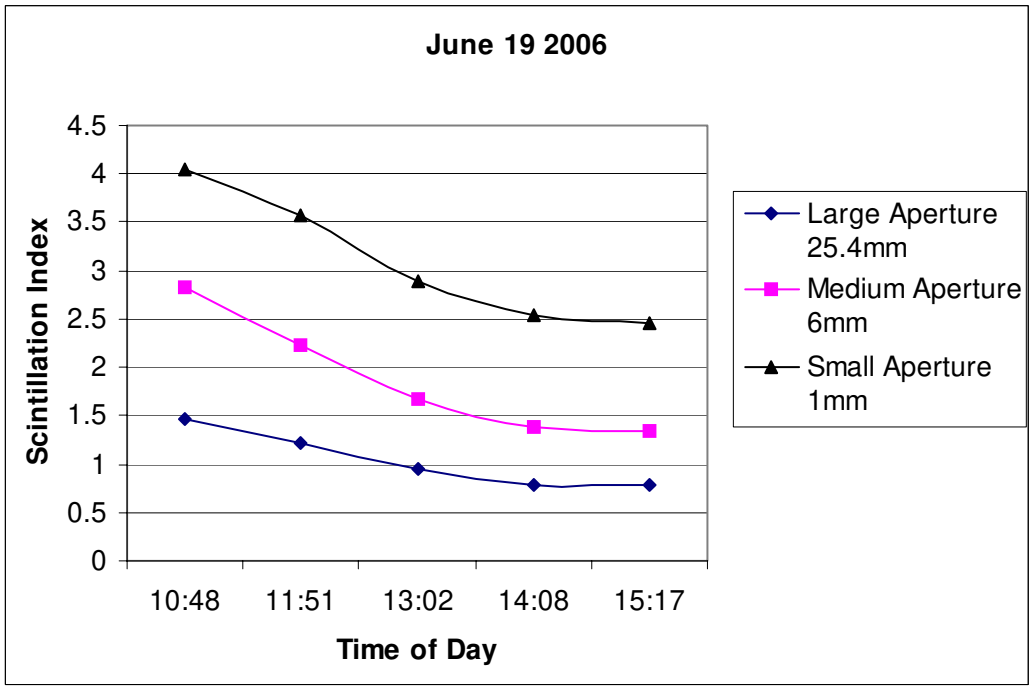

Figure 17: Scintillation indices using final values of three-aperture sizes.

Inferring C_n^2, l_0, L_0

The data from the days of June 05 2006 and June 19 2006 were used to infer values for C_n^2, l_0, L_0. These days were chosen based upon the strong turbulence that occurred, the height of the BLS900, and the use of different aperture sizes for each day.

Calculated scintillation indices from the three apertures were entered into the custom Mathematica program. The program performed two minimizations to calculate the three atmospheric parameters. The first minimization was done with an exponent value of $p = 2$ in equation (39); it was used to get a stable value for C_n^2. Values for inner and outer scale were also calculated, but discarded because $p > 1$ gives unstable solutions for inner and outer scale.[8] The C_n^2 value from the first minimization was then used as an input to the second minimization. A value of $p < 1$ was required in order to get stable solutions for l_0 and L_0, therefore $p = ¼$ was chosen. Due to the strong turbulence on both these days, the spacing of the scintillation indices was great enough to allow for converging solutions. On average, the Mathematica program converged on solutions for the three atmospheric parameters within a minute. If the program ran for longer than five minutes, it was aborted under the assumption that a stable solution could not be reached.

C_n^2 Comparison

Figure 18 and Figure 19 below compare the seven one-minute average C_n^2 values calculated with the three-apertures and the average of the seven one-minute values measured by the BLS900 on June 05 2006 and June 19 2006.

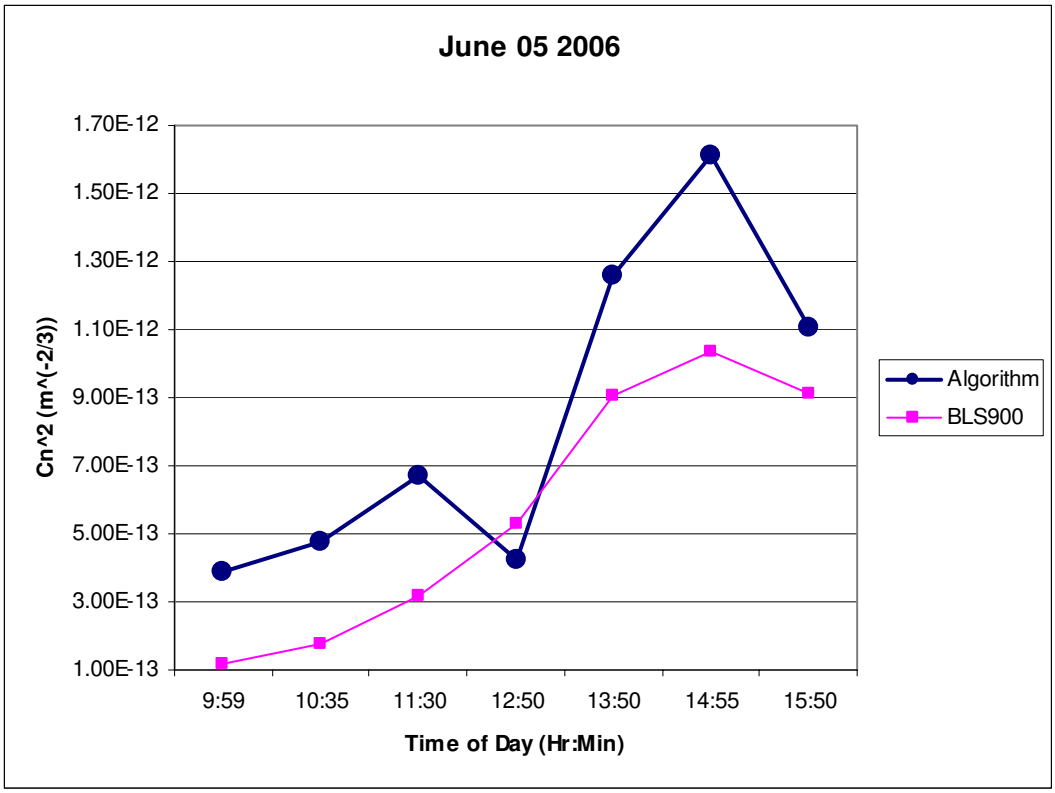

Figure 18: Calculated and measured C_n^2 for June 05 2006.

Typically, the calculated C_n^2 was higher than that measured by the BLS900. The plot for June 05 2006 follows such a trend, except for an outlier at 12:50. The drop in C_n^2 at that point was most likely caused by a rain shower which occurred around 12:15.

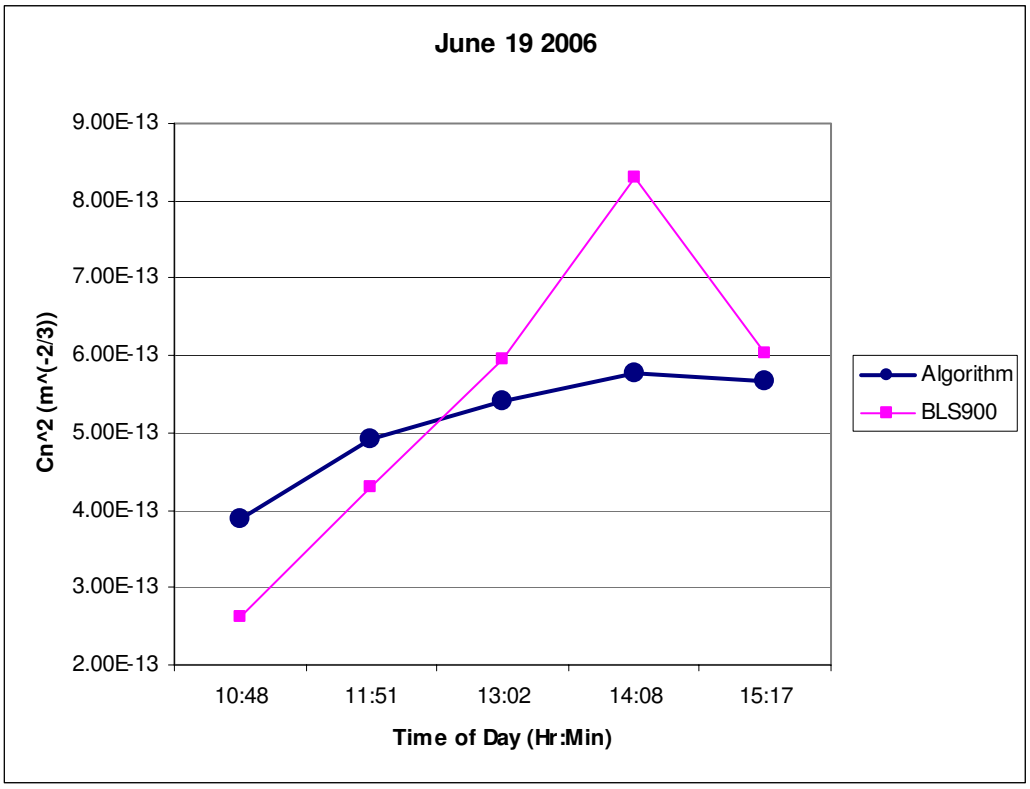

Figure 19: Calculated and measured C_n^2 for June 19 2006

The plot for June 19 2006 does not exhibit the same trend. However, the plot of calculated C_n^2 is much smoother than that measured from the BLS900. This implies that the BLS900 may be in error for some of its values. It should be noted that on either day, the three-aperture setup and the BLS900 were separated by a distance larger than a Fresnel zone. This resulted in each instrument seeing a statistically different section of atmospheric turbulence. On average over the two days, the calculated C_n^2 was 21% higher than that measured by the BLS900. This follows the results from the experimentation performed in 2004 in *Scintillation: theory vs. experiment*.

Scintillation Index Comparison

From the data collected and the theory developed by Andrews *et al.,* scintillation indices were calculated based upon the three aperture sizes. Although the BLS900 did not output scintillation index, it was inferred using the custom Mathematica program. Using the C_n^2 measurement from the BLS900 as an input to the algorithm, keeping all other parameters the same, and only performing the second minimization of the Mathematica program, values for l_0 and L_0 were obtained corresponding to the C_n^2 of the BLS900. The scintillation index for the BLS900 was then calculated using the theory of Andrews *et al*. The scintillation index values were inferred based upon the assumption that the BLS900 provided a correct representation of the path averaged C_n^2. Figure 20 outlines the process of inferring scintillation indices for the BLS900.

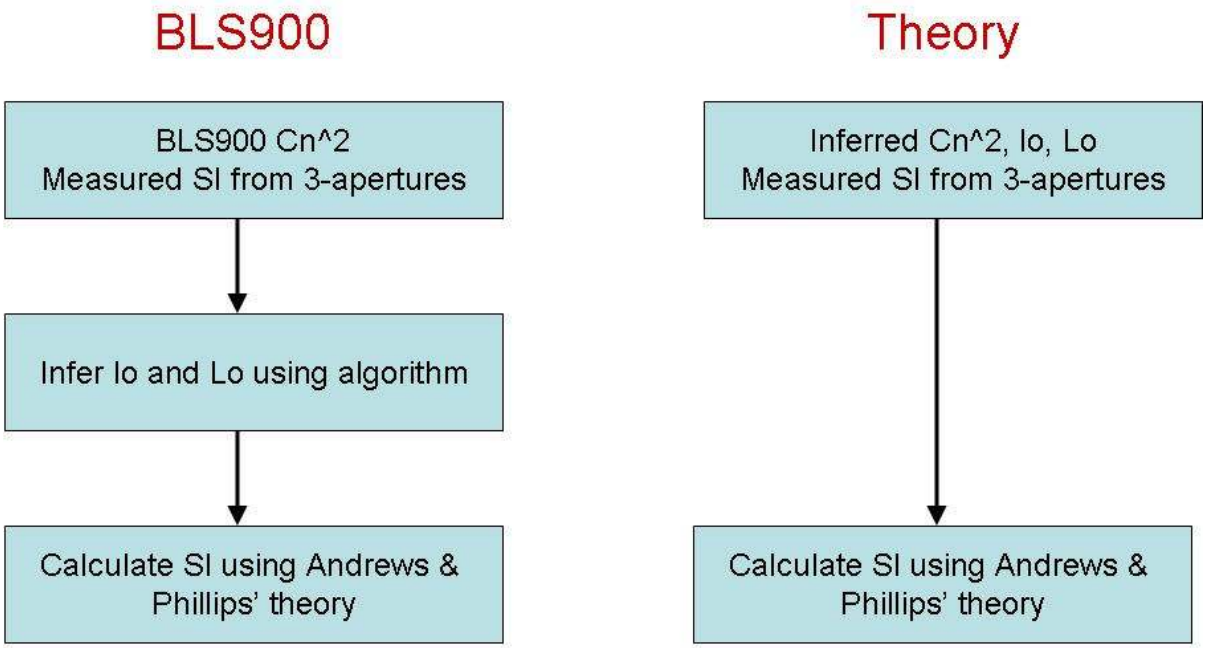

Figure 20: Inferring scintillation index from theory.

Figure 21, Figure 22, and Figure 23 compare the scintillation indices measured from the collected data, the theoretical scintillation indices based upon the C_n^2 from the collected data, and the theoretical scintillation indices based upon the C_n^2 reported by the BLS900. The data were collected on June 05 2006 using aperture sizes of 25.4mm, 10mm, and 1mm.

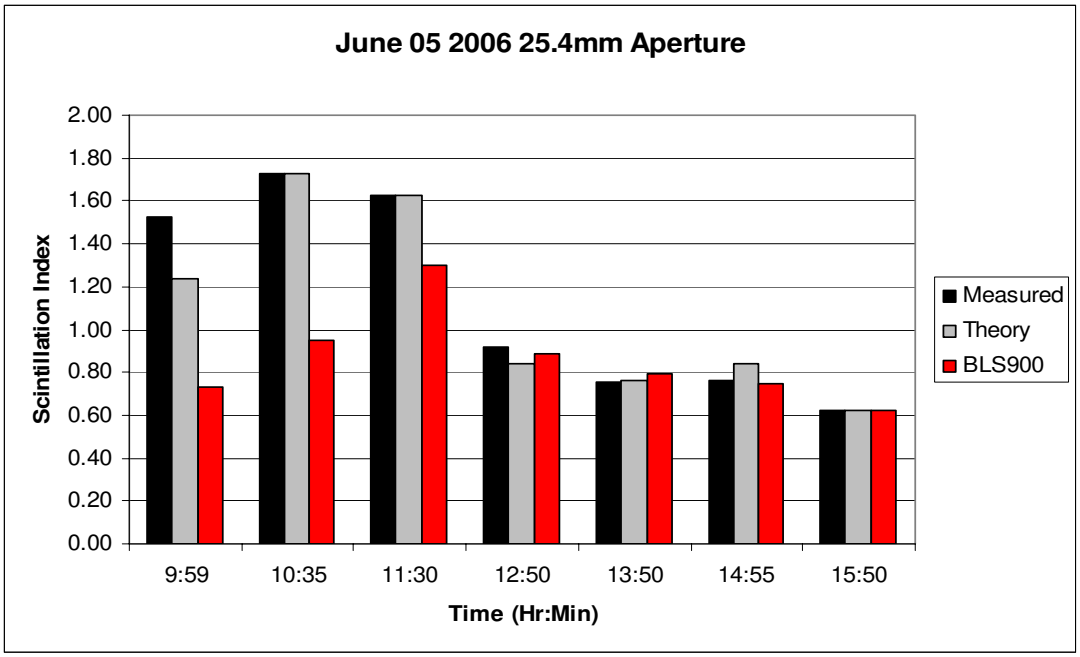

Figure 21: Scintillation indices from June 05 2006 using a 25.4mm aperture.

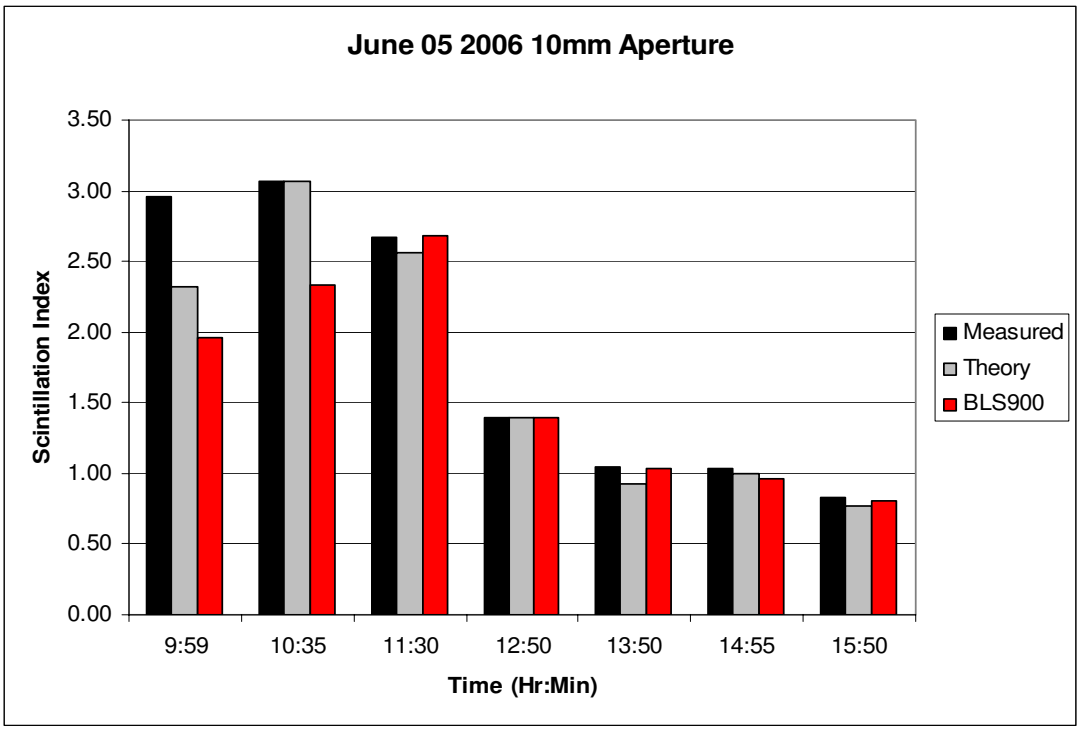

Figure 22: Scintillation indices from June 05 2006 using a 10mm aperture.

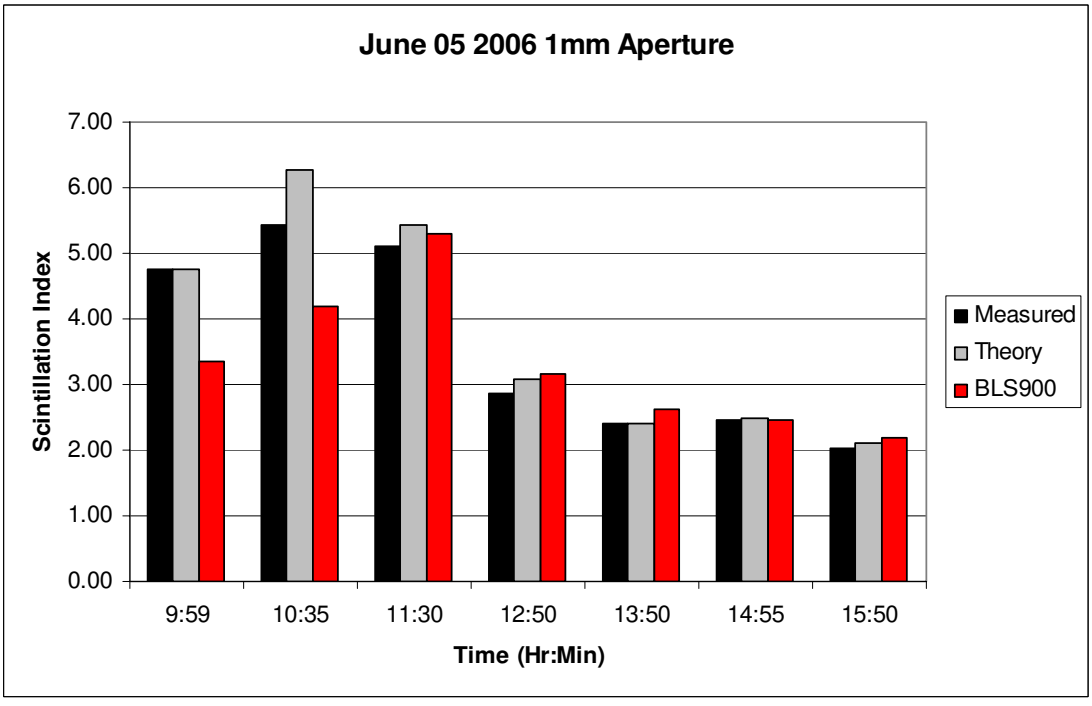

Figure 23: Scintillation indices from June 05 2006 using a 1mm aperture.

Figure 24, Figure 25, and Figure 26 compare the scintillation indices measured from the collected data, the theoretical scintillation indices based upon the C_n^2 from the collected data, and the theoretical scintillation indices based upon the C_n^2 reported by the BLS900. The data were collected on June 19 2006 using aperture sizes of 25.4mm, 6mm, and 1mm.

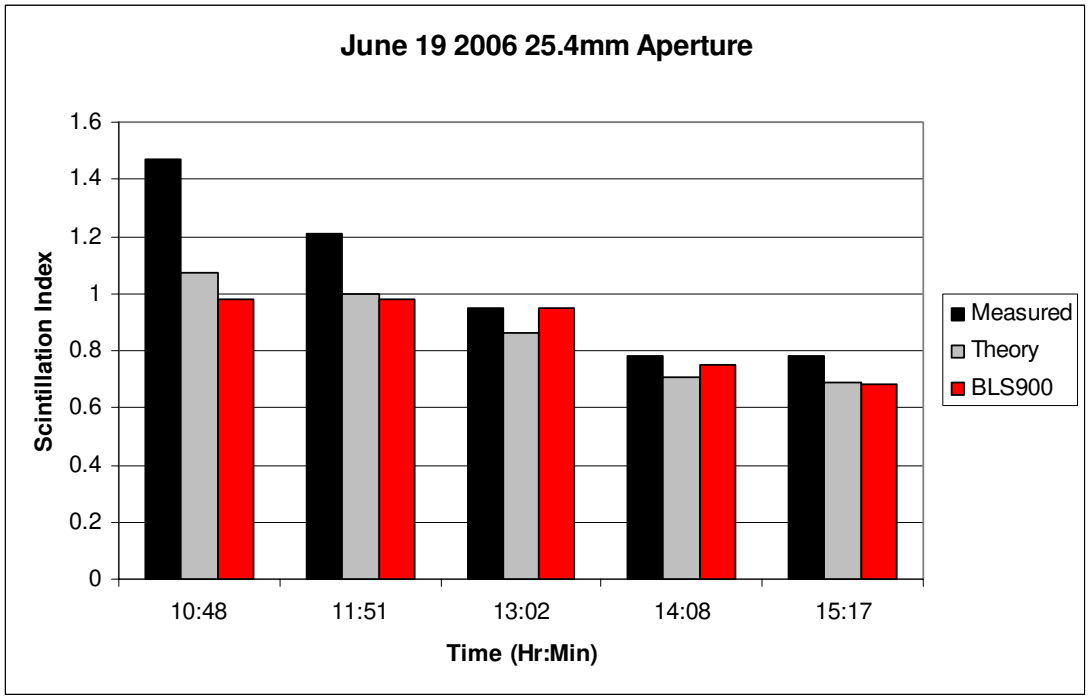

Figure 24: Scintillation indices from June 19 2006 using a 25.4mm aperture.

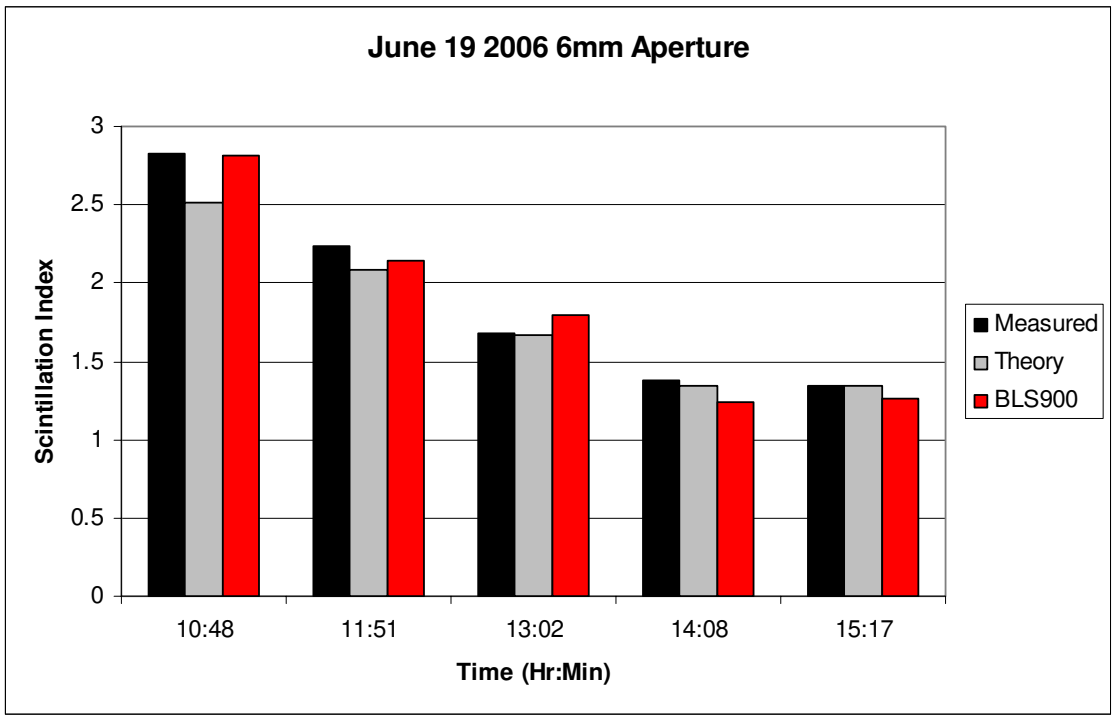

Figure 25: Scintillation indices from June 19 2006 using a 6mm aperture.

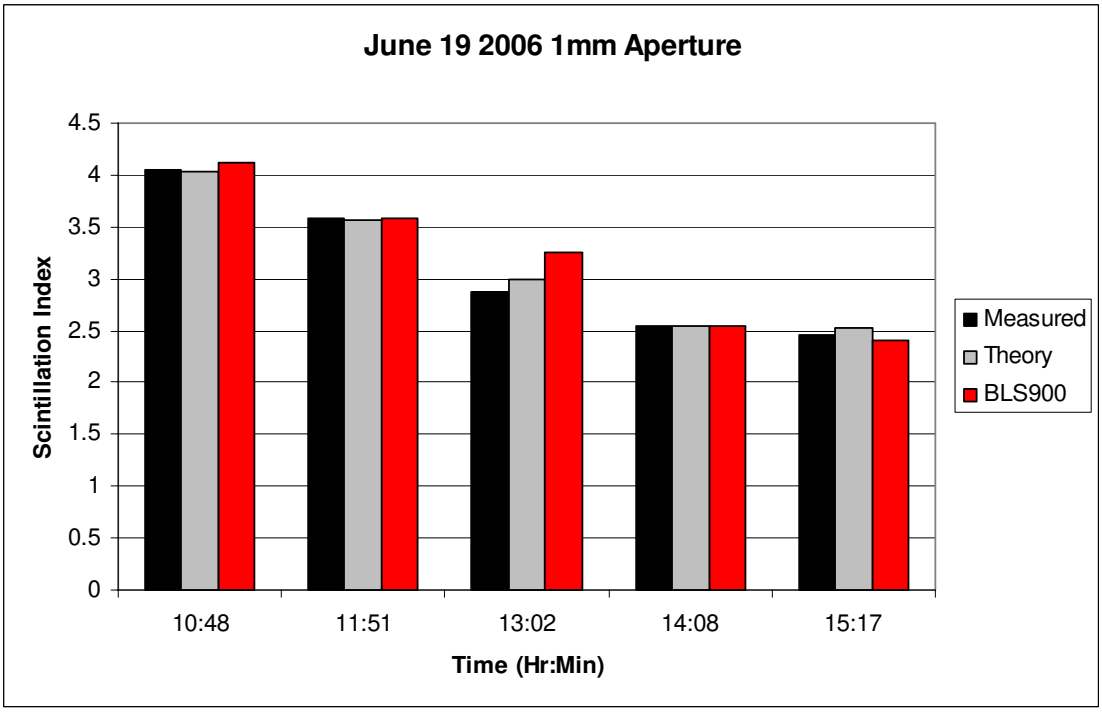

Figure 26: Scintillation indices from June 19 2006 using a 1mm aperture.

From 9:59 to 10:35 on June 05 2006, the BLS900 predicted low scintillation indices compared to the theory and calculated values. The BLS900 values came closer to the experimental data scintillation index once the turbulence decreased. This trend was seen due to the BLS900 using a look-up table to compensate for strong irradiance fluctuations. As stated in the background section, the BLS900 was designed to be relatively insensitive to strong fluctuations due its aperture size being an order of magnitude larger than the inner scale and an order of magnitude smaller than the outer scale. The developed theory takes the strong fluctuations into account and thus can make a more accurate prediction to the experimental data. Overall, the theory came closer to estimating the experimental scintillation index than the BLS900. Table 4 shows the percent difference of the scintillation index (SI) with respect to the calculated value from the experimental data.

Table 4: Scintillation index percent difference for June 05 2006 and June 19 2006.

SI Measurement	% Difference for June 05 2006	% Difference for June 19 2006	Net % Difference
Theoretical SI for Large Aper.	3.52	16.66	8.72
Theoretical SI for Middle Aper	7.40	5.36	6.54
Theoretical SI for Small Aper	5.97	1.25	4.17
BLS900 SI for Large Aper	24.05	16.47	21.05
BLS900 SI for Middle Aper	14.01	2.18	9.03
BLS900 SI for Small Aper	7.16	2.67	3.41

The percent difference from the theory was typically smaller than that of the BLS900. Over the two days, the difference within the theoretical predictions was consistent and less than 9%. This illustrates the validity and stability of the theory.

l_0 and L_0 Comparison

Using the scintillation indices from the previous section, inner and outer scales values for the experimental data and the BLS900 were realized with the Mathematica program. Again, the BLS900 did not output a value for inner or outer scale, but solutions were inferred using the C_n^2 as an input to the second minimization of the Mathematica program. The inner scale was also calculated using a method developed by Hill.[4] Figure 27 and Figure 28 show the inner scale of turbulence calculated using the experimental data and calculated using the BLS900 measurements from June 05 2006 and June 19 2006. The calculations were performed over 7-minute periods to suppress the fluctuations seen from minute-to-minute.

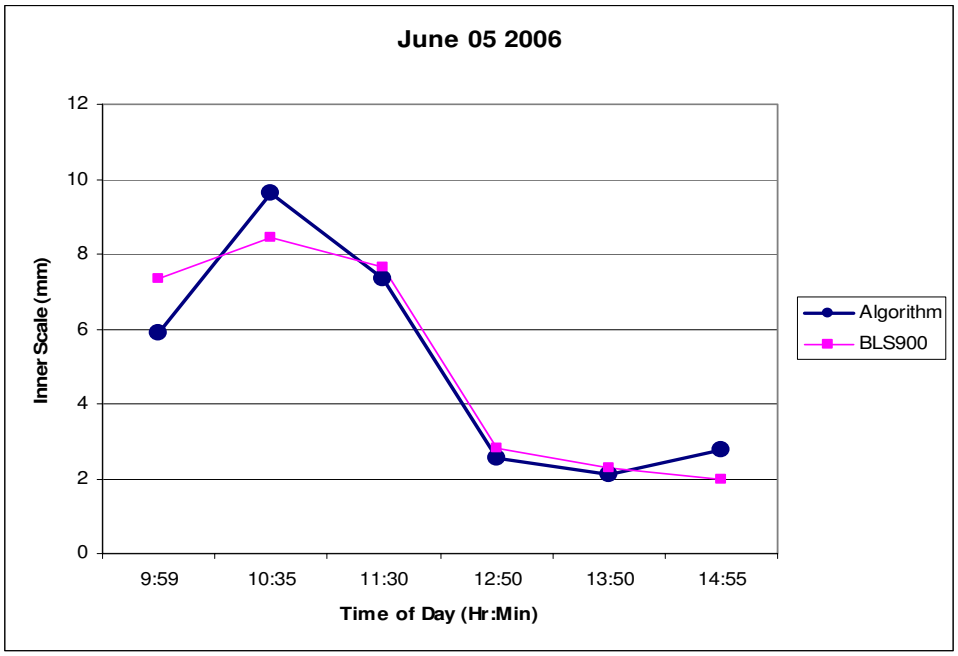

Figure 27: Inner scale profile over 7-minute average intervals from experimental data on June 05 2006.

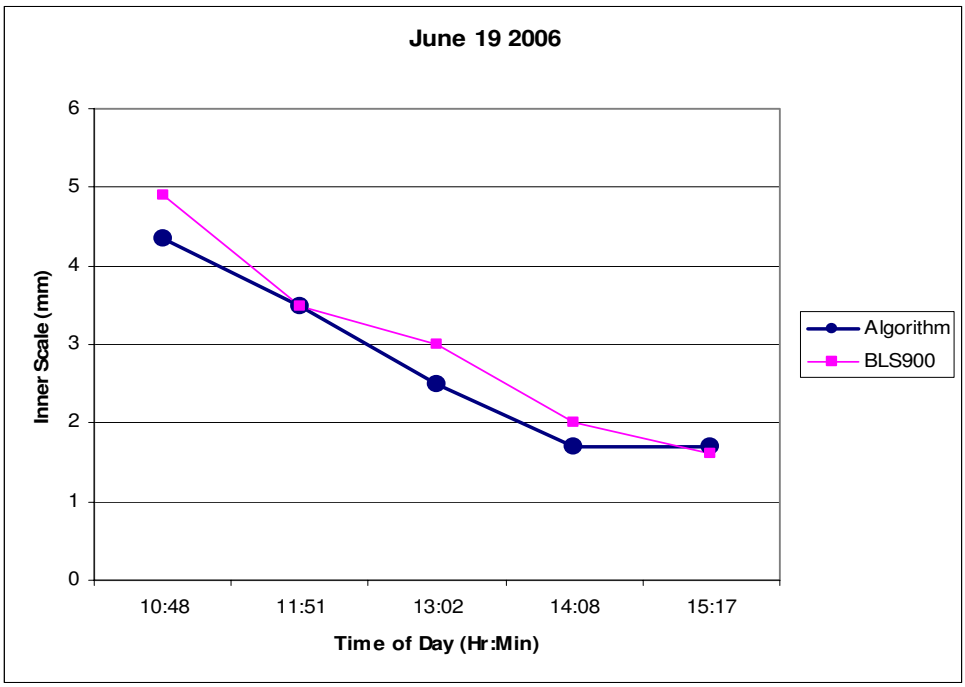

Figure 28: Inner scale profile over 7-minute average intervals from experimental data on June 19 2006.

Both days yielded reasonable results for l_0. The stability of the solutions was checked by varying the exponent, p, in the second minimization of the Mathematica program. It was discovered by experiments performed in 2005 that the second minimization needed to have an exponent less than one to find a unique solution for the inner and outer scale.[8] For those experiments, $p = 1/4$ was chosen. When calculating values for these experiments, the exponent was varied between $1/8$ and $1/2$. Since the spread in aperture sizes was much larger than that of previous experiments, changing the exponent had little effect on the solution. The inner scale solutions were accurate within 0.5mm, depending on the value of p. This verified the stability of the inner scale solutions from the downhill simplex method.

Using Hill's model for l_0 based upon path-averaged wind speed, surface roughness, and path height, comparisons were made with the l_0 inferred from the three-aperture data and the BLS900; see equation (37). In Figure 29, the l_0 calculated from the experimental data using the Mathematica program is plotted with the l_0 calculated using Hill's model. These calculations are performed over 7-minute intervals on June 05 2006. The wind speed was obtained from the anemometer of the weather station.

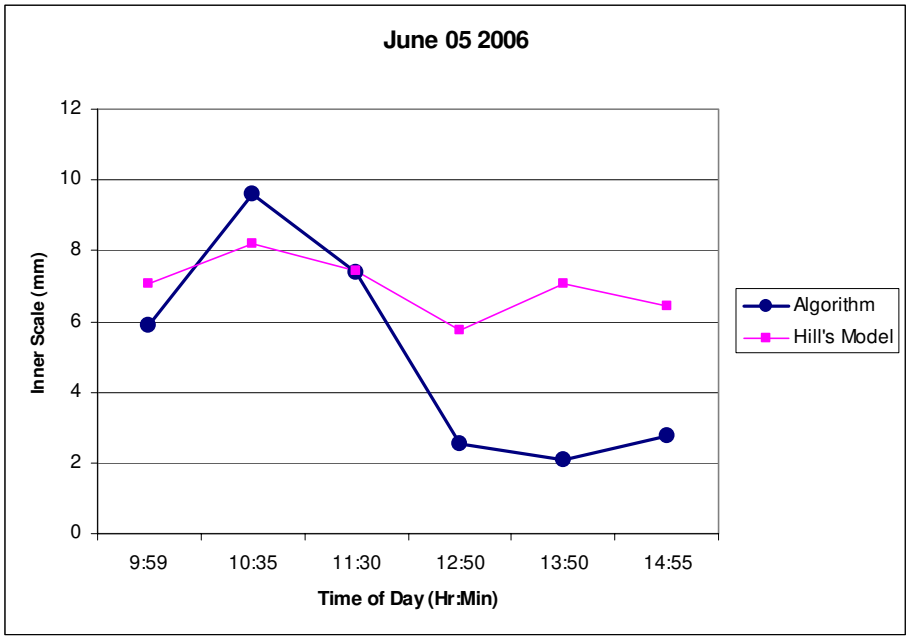

Figure 29: Comparison between inner scale values calculated from experimental data and Hill's model for June 05 2006.

The first three data runs on June 05 2006 yielded high values for l_0 using the downhill simplex minimization. Hill's model was able to follow the trend of the first three data points closely. The model was not as accurate for the last two data points. The 4mm drop in l_0 at 12:50 was most likely due to a rain shower occurring at 12:15. Figure 30 shows a similar plot, only for data collected on June 19 2006.

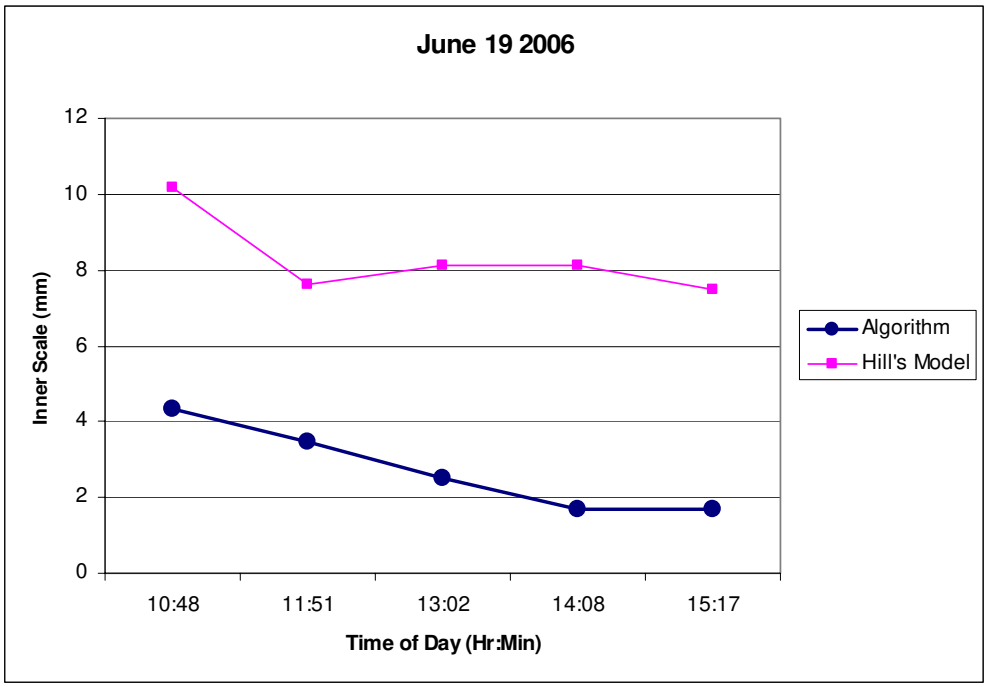

Figure 30: Comparison between inner scale values calculated from experimental data and Hill's model for June 19 2006.

The l_0 data from June 19 2006 consisted of values below 5mm, as inferred using the Mathematica program. Hill's model predicted larger inner scale values than those inferred through the algorithm. The trends of the inner scale are similar, but offset roughly 6mm.

Figure 31 and Figure 32 show the outer scale of turbulence calculated using the experimental data and calculated using the BLS900 measurements from June 05 2006 and June 19 2006. The calculations were performed over 7-minute periods to suppress the fluctuations seen from minute-to-minute. It should be noted in Figure 31 that an outer scale of 3m corresponds to $L_0 = \infty$. This mapping was done to keep the axis of the plot reasonable.

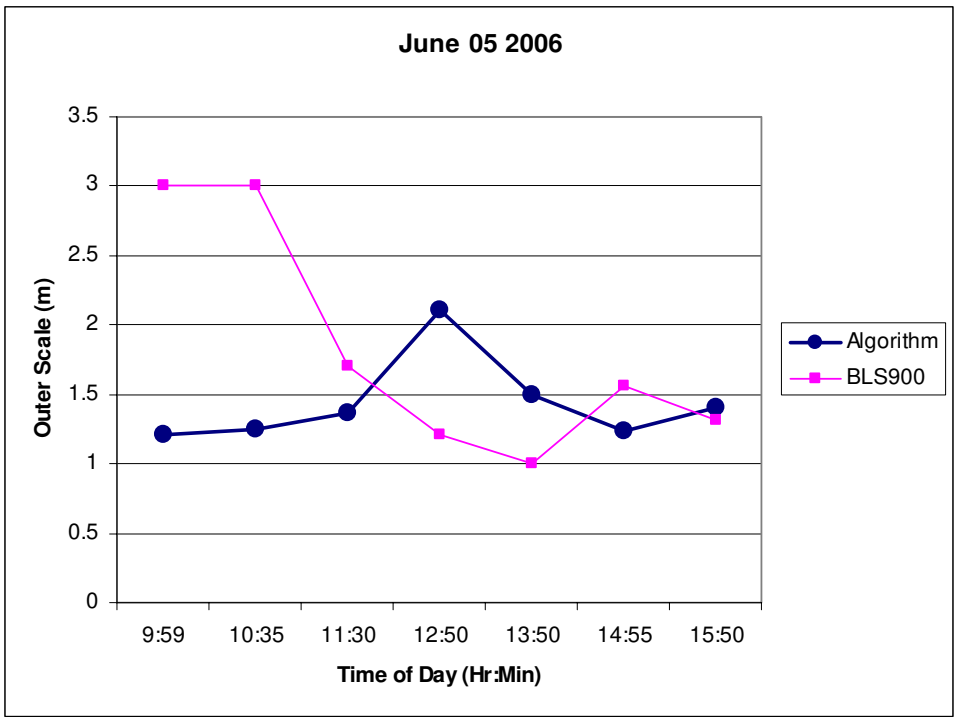

Figure 31: Outer scale profile over 7-minute average intervals from experimental data on June 05 2006.

The L_0 values from June 05 2006 do not follow the same trend. The first two data points of the BLS900 indicate an infinite outer scale. An infinite outer scale implies weak fluctuations, which according to the scintillation index of the experimental data was not the case. At 12:50 the calculated L_0 reached a peak value, this was most likely due to the cooling of the ground by a rain shower at 12:15.

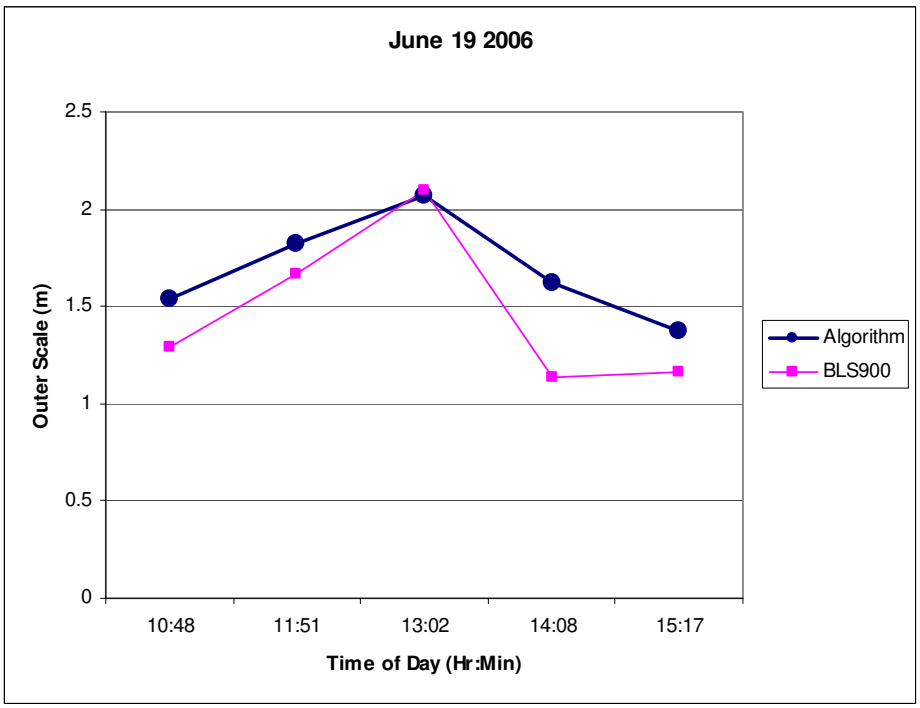

Figure 32: Outer scale profile over 7-minute average intervals from experimental data on June 19 2006.

On June 19 2006, the two data sets seem to follow one another well. As a rough estimate, L_0 is typically half the height of the propagation path during strong turbulence;[3] 1m for these experiments. Therefore, the values inferred from both days are reasonable solutions. Both days the outer scale followed a trend of starting and ending at about the same value and reaching a peak around solar noon.

Overall, the data presented from June 19 2006 had better results. The trend for the C_n^2 was smoother, the scintillation indices matched the theory better, and the inner scale values illustrated a smooth change and matched the trend of Hill's model. The data may have been better due to the skies being clear and consistent throughout the day. Also, it may have been due to the aperture size being used on June 19 2006 was 6mm; thus giving the best separation between the

scintillation indices. Hill's model did a reasonable job predicting the trend of the inner scale based upon the path-averaged wind speed. In the next section, the algorithm used to calculate the crosswind speed is discussed.

Crosswind Speed

Data Processing

The crosswind speed was found by taking the time-lagged cross-correlation of the two recorded signals. The cross-correlation was used as opposed to the cross-covariance based on the assumption of constant mean background intensity and a stationary mean during the data run. The cross-correlation was then smoothed using a moving average, normalized, and plotted against the delay time. A custom program was written in Matlab to perform the calculations (APPENDIX B). The program used the irradiance data from the two PMTs as inputs. It then separated the data into one-minute segments and calculated the time-lagged cross-correlation for each minute. The program was verified with two square wave test signals, offset by a known time delay. The crosswind speed for each minute was calculated along with a seven-minute crosswind speed computed from the average of the individual one-minute cross-correlations. The time when the peak of the cross-correlation plot occurred was then used in calculating the crosswind speed. Equation (42) shows the formula used

$$\bar{u} = \frac{Separation\ Dis\tan ce}{Delay\ Time}, \tag{42}$$

where the separation distance is the spacing between the centers of the PMT apertures and the delay time is the time when the peak cross-correlation occurs. Plots of the cross-correlation for different aperture and separation distances were compared to determine the ideal setup. The crosswind speed values obtained experimentally were compared with those of the BLS900 commercial scintillometer and the anemometer of the weather station.

Comparison

The calculated crosswind speed from the PMTs did not match the values recorded from the BLS900 or the weather station anemometer. The calculated values were typically larger compared to those from the BLS900 and the anemometer. Since the BLS900 provided a path averaged crosswind speed, unlike the point measurement of the anemometer, its values were expected to match the calculated crosswind speed more so than the anemometer.

To begin, the distance between the apertures was kept at 120mm, as this was the spacing used to collect scintillation index data. The aperture sizes were switched between the two available sizes, 1mm and 25.4mm. Figure 33 and Figure 34 show the cross-correlation plots from July 11 2006 for the 1mm and from July 13 2006 for the 25.4mm aperture. A moving average with a

window of 14 samples was used for smoothing. This window size proved to average out the majority of noise, while still retaining accuracy of the peak's occurrence time.

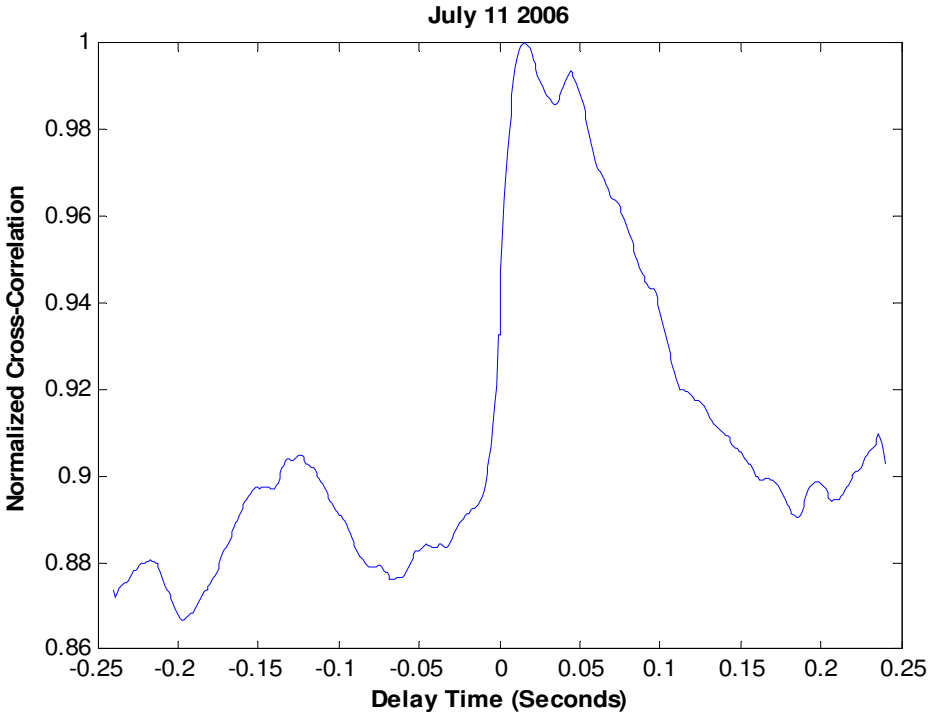

Figure 33: Cross-correlation of intensity fluctuations using a 1mm aperture and 120mm separation.

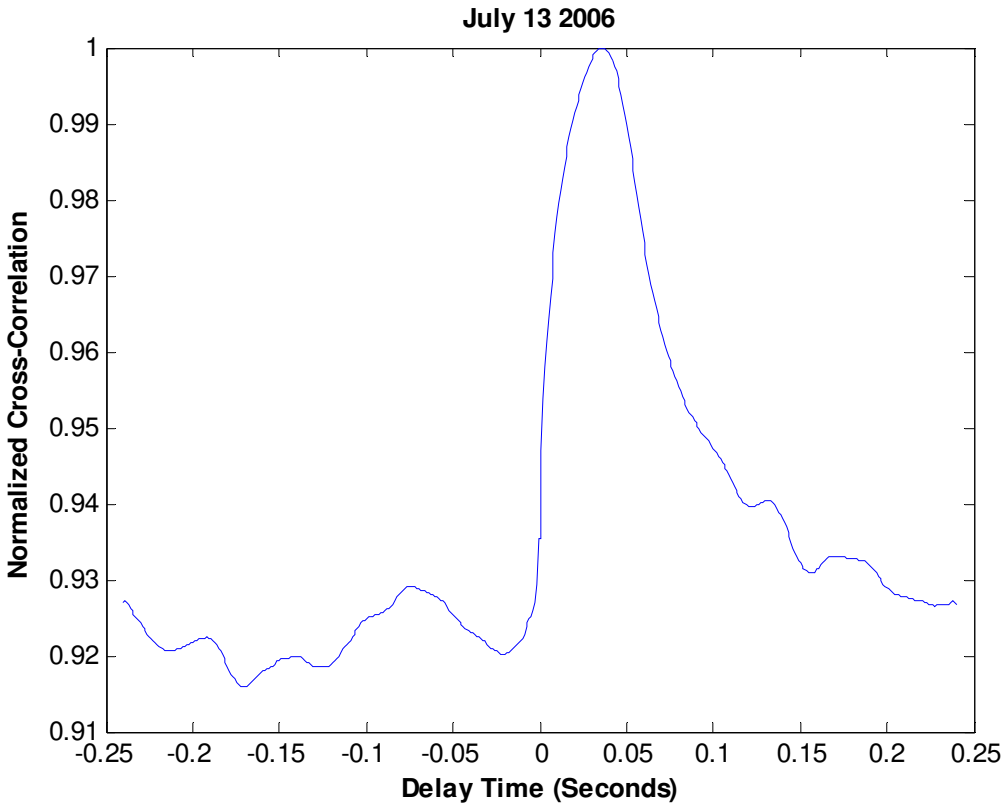

Figure 34: Cross-correlation of intensity fluctuations using a 25.4mm aperture and 120mm separation.

From the plots above, it is obvious that the 1mm aperture is much noisier than the 25.4mm aperture. This is due to the aperture size being smaller than the average scale size, l_0, blowing across it. The larger aperture is able to have more than one eddy in its field of view, thus experiencing an aperture averaging effect. The averaging effect produces a much smoother cross-correlation plot with a single well defined maximum.

Next the apertures were fixed at 25.4mm and the separation distance was varied between 70mm and 178mm. Figure 35, Figure 36, and Figure 37 show the normalized cross-correlation data

collected on July 13 2006 with separation distances of 70mm, 120mm, and 178mm, respectively. A moving average with a window of 14 samples was used for smoothing.

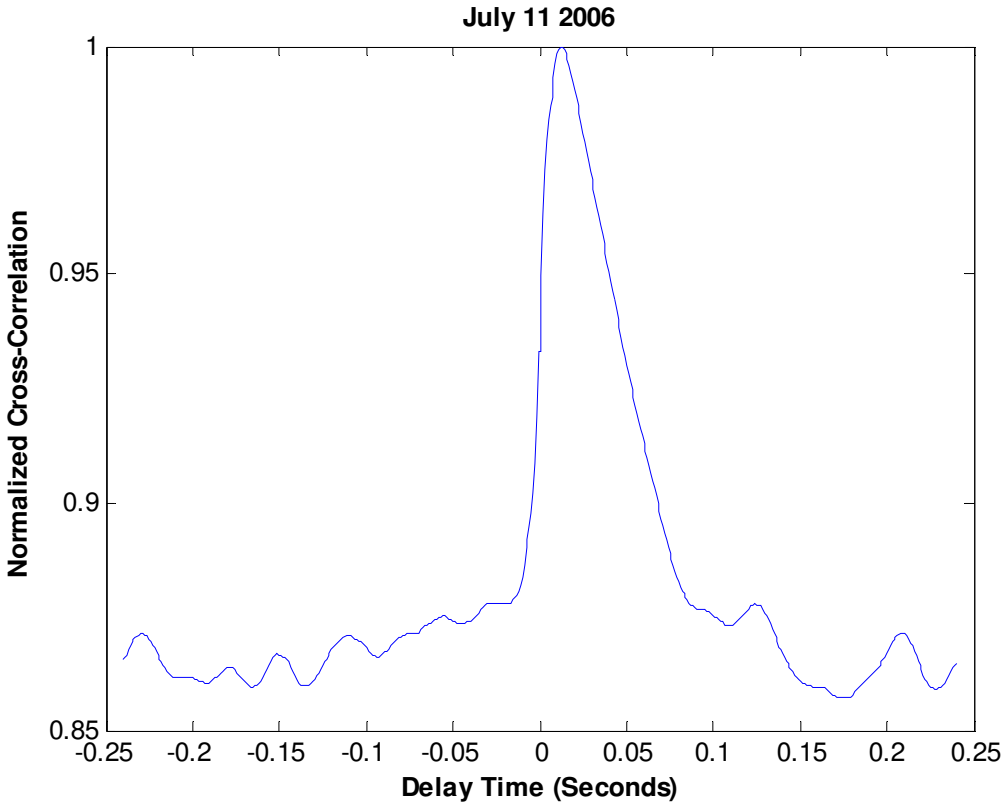

Figure 35: Cross-correlation of intensity fluctuations using a 25.4mm aperture and 70mm separation.

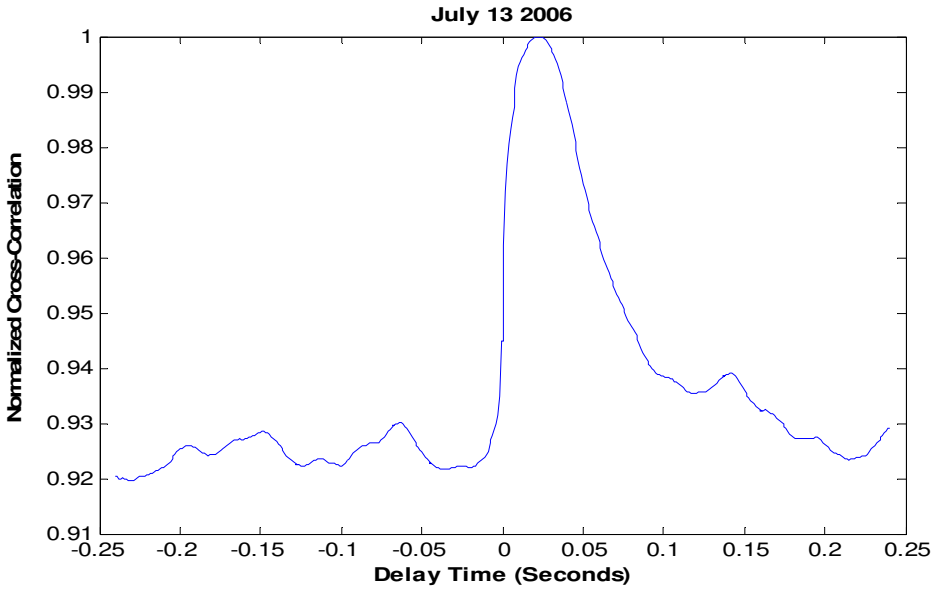

Figure 36: Cross-correlation of intensity fluctuations using a 25.4mm aperture and 120mm separation.

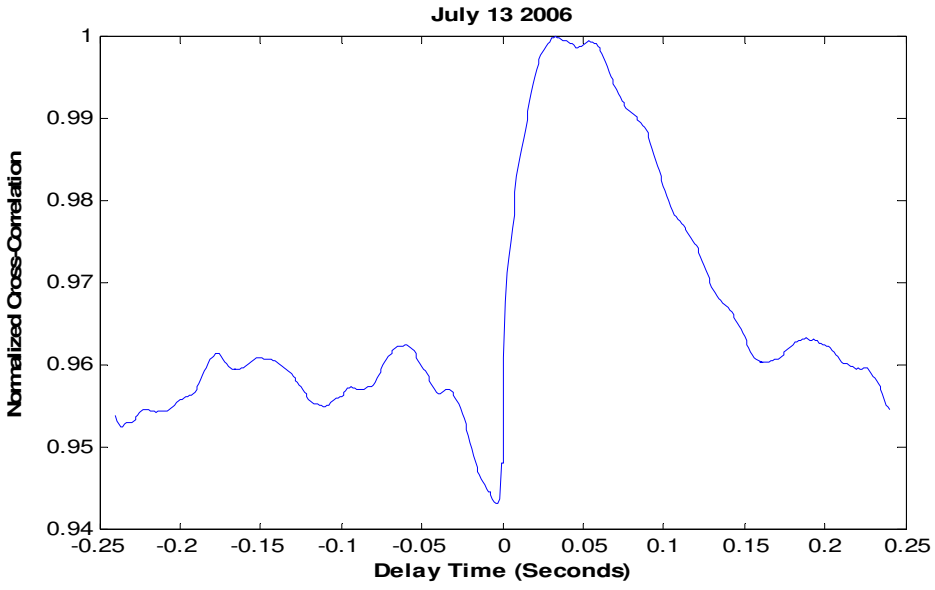

Figure 37: Cross-correlation of intensity fluctuations using a 25.4mm aperture and 178mm separation.

As the separation distance increased, the peak became more spread. A plot similar to Figure 35 is desired to accurately identify the maximum value.

The crosswind direction can also be determined whether the delay time is positive or negative. Referring to Figure 14, a positive time delay corresponds to the crosswind blowing from PMT1 to PMT2 (East to West). The crosswind directions calculated from the experimental data match the direction reported by the BLS900. They do not match the direction measured by the anemometer; this is expected because the anemometer is a point measurement and is more susceptible to instantaneous changes.

The following plots compare the crosswind speed obtained using the cross-correlation with that measured by the BLS900 and the anemometer. Figure 38 shows the 7-minute data run which had the best trend fit to the BLS900 and the anemometer. The data were collected on July 13 2006 at 14:02 with 25.4mm apertures spaced 120mm apart.

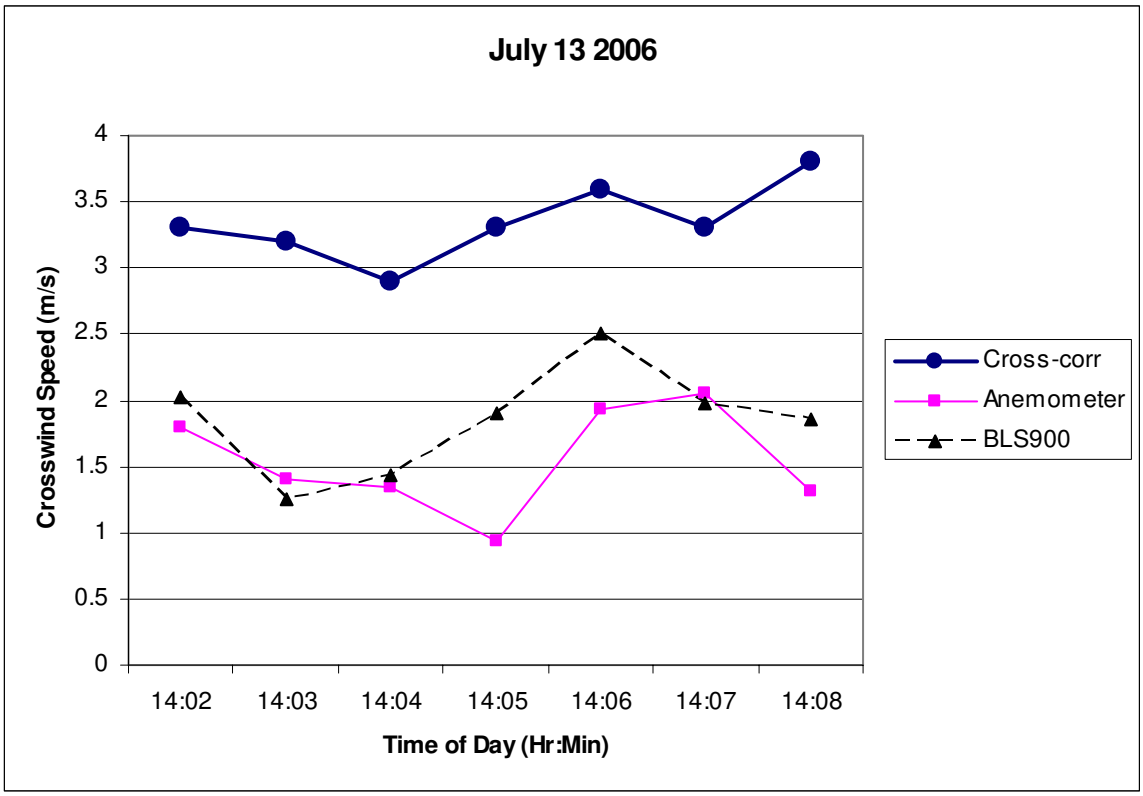

Figure 38: Calculated crosswind speed comparison showing best fit to anemometer and BLS900.

Figure 39 shows the 7-minute data run that was setup using the conclusions above; 25.4mm aperture and 70mm spacing. The data were collected on July 11 2006 at 15:39 with 25.4mm apertures spaced 120mm apart.

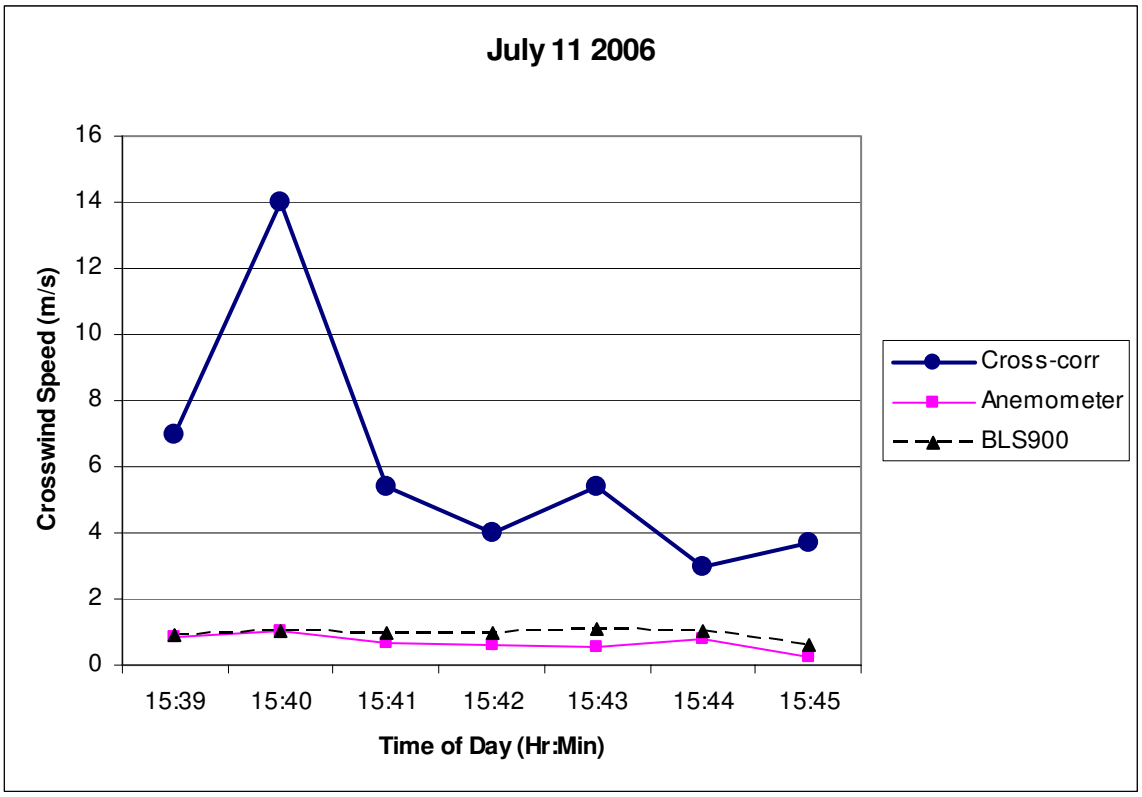

Figure 39: Calculated crosswind speed comparison using ideal configuration.

The data collection system was configured differently on July 11 and 13 2006, therefore 7-minute averages were not plotted. Data runs throughout those days were taken with different aperture size and separation configurations, which yielded a misrepresentation of the day's crosswind speed. Figure 38 illustrates a correlation between the experimental data and the BLS900. Although the experimental data is consistently higher than the BLS900, it follows the same trend. Figure 39 shows the experimental data almost following the trend of the BLS900; the main difference is due to an outlier at 15:40. The crosswind speed calculated through the cross-correlation of the experimental data always yielded higher crosswind speed values than that of the anemometer or the BLS900.

There are many factors that could have caused the large discrepancy between the calculated crosswind speed and those recorded by the BLS900 and the weather station anemometer. Aperture averaging could have influenced the calculated crosswind speed. The BLS900 uses two 150mm transmitters and a 145mm receiver. The largest receiver used in the experimental data collection was 25.4mm. A larger aperture size was not used due to the limitation of the active area of the PMT. Another source of difference could have been the spacing of the apertures. The BLS900 has 214mm spacing between the two transmitters. Although data was collected at a minimum separation of 70mm and a maximum separation of 178mm, different aperture spacing may have been needed. The range of separation above was limited by the size of the PMT enclosures and the optical table. The difference in vertical height of the BLS900 and the PMT apertures may have contributed to the difference. The BLS900 and the weather station anemometer were positioned above the foliage at 2.5m and 3.3m, respectively, while the PMT apertures were positioned at 1.6m. The top of the foliage at the ISTEF range stopped around 2.0m. The foliage was expected to reduce the crosswind speed, thus the BLS900 should have yielded a higher crosswind speed than that calculated. Due to restrictions on the optical table, the BLS900 and the PMTs could not be mounted at the same height above the ground. The other possibility for difference would be in the data collection. The data was collected at 1,000 samples/sec, but that might not have been fast enough in strong turbulence. If under-sampling occurred, then aliasing of the signal would have led to an incorrect reproduction of the sampled atmosphere.

CHAPTER 6: CONCLUSION

Accomplishments

Collecting irradiance fluctuations and inferring atmospheric turbulence parameters were the main focus of this research. A review of currently available techniques to extract certain atmospheric parameters was presented. The experimental setup and data collection process was explained for the three-aperture experiment. The optimal aperture sizes for the three-aperture experiment were presented. The scintillation index was calculated and compared for experimental data, theory developed by *Andrews et. al*[2], and the BLS900. Based upon those scintillation indices, C_n^2, l_0, and L_0 were inferred using the downhill simplex method. Results from the experimental data matched the theory closely. Results from the BLS900 did not offer the same stability as the theory.

The data collection and processing for the crosswind speed was discussed. Cross-correlation plots for different equipment configurations were presented, arriving at the ideal arrangement. A large receiving aperture and small separation distance yielded the best cross-correlation plot. The crosswind speed calculated from the experimental data was compared with that of the path averaged value from the BLS900 and point measurement from the anemometer. The crosswind speed from the experimental data was consistently higher than the other two measurements. Reasons for these differences were presented.

Future Work

Although there were many useful conclusions drawn in this thesis, future work still remains. The transmitter and receiver of the commercial scintillometer should be placed within a Fresnel zone of the three-aperture transmitter and receiver. The two systems will then see statistically equivalent turbulence. A variable middle aperture will allow for the best separation between scintillation index curves. This will increase the chances of converging solutions from the minimization program. As the software of the BLS900 is periodically updated, a new feature will be available to view the unprocessed data of the scintillometer. This raw data will allow for a more accurate comparison between the BLS900 and the three-aperture data. A modulated and pulsed laser transmitter for the three-aperture system will yield more accurate irradiance measurements because the instantaneous background can be subtracted from the signal. Finally, a larger aperture size, at least 100mm, for the three-aperture system will give increased stability of the inner and outer scale values.

APPENDIX A
DERIVATION OF LOG-IRRADIANCE TERMS

This derivation is followed from the work done in *Characterizing the propagation path in moderate to strong optical turbulence.* At the transmitter, a Gaussian beam wave is defined in terms of the beam radius, W_0, and the phase front radius of curvature, F_0. These parameters are related to the (hard) transmitter aperture diameter, d, and the half-angle transmitter beam divergence θ_{div} according to

$$W_0 = \frac{d}{2\sqrt{2}} \tag{A1}$$

and

$$F_0 = -\frac{W_0}{\theta_{div}}. \tag{A2}$$

A propagating beam is characterized by the beam parameters, which in the transmitting plane are defined by[3]

$$\Theta_0 = 1 - \frac{L}{F_0} \tag{A3}$$

and

$$\Lambda_0 = \frac{2L}{kW_0}, \tag{A4}$$

where L is the propagation distance and k is the optical wave number. At the receiver, located at distance L, the receiver beam parameters are defined by[3]

$$\Theta = \frac{\Theta_0}{\Theta_0^2 + \Lambda_0^2}, \tag{A5}$$

$$\overline{\Theta} = 1 - \Theta, \tag{A6}$$

and

$$\frac{\Lambda_0}{\Theta_0^2 + \Lambda_0^2}. \tag{A7}$$

The theoretical expression for the scintillation index of a receiver with aperture diameter D is a function of C_n^2, l_0, L_0, and D[3]

$$\sigma_I^2\left(l_0, L_0, C_n^2, D\right) = \exp\left[\sigma_{\ln x}^2\left(l_0, C_n^2, D\right) - \sigma_{\ln x}^2\left(l_0, L_0, C_n^2, D\right) + \sigma_{\ln y}^2\left(l_0, C_n^2, D\right)\right] - 1 \tag{A8}$$

where $\sigma_{\ln x}^2$ and $\sigma_{\ln y}^2$ are large-scale and small-scale log-irradiance scintillation, respectively. As shown in equation (A8), $\sigma_{\ln x}^2$ can be divided into two terms, where the outer-scale dependence is fully captured in the second term. For mathematical convenience, the following dimensionless quantities that depend on C_n^2, l_0, L_0, and D are introduced:[3]

$$Q_l(l_0) = \frac{10.89L}{kl_0^2}, \tag{A9}$$

$$Q_0(L_0) = \frac{64\pi^2 L}{kL_0^2}, \tag{A10}$$

$$\sigma_I^2\left(C_n^2\right) = 1.23C_n^2 k^{7/6} L^{11/6}, \tag{A11}$$

$$\Omega_G(D) = \frac{16L}{\kappa D^2}. \tag{A12}$$

The first part of $\sigma_{\ln x}^2$ does not depend on the outer scale of turbulence, L_0. For an on-axis portion of a Gaussian beam wave, it is defined by[3]

$$\sigma_{\ln x}^2\left(l_0, C_n^2, D\right) = 0.49\sigma_I^2\left(\frac{\Omega_G - \Lambda}{\Omega_G + \Lambda}\right)\left(\frac{1}{3} - \frac{1}{2}\overline{\Theta} + \frac{1}{5}\overline{\Theta}^2\right)\left(\frac{\eta_{xd}Q_l}{\eta_{xd} + Q_l}\right)^{7/6} \times \left[1 + 1.75\left(\frac{\eta_{xd}}{\eta_{xd} + Q_l}\right)^{1/2} - 0.25\left(\frac{\eta_{xd}}{\eta_{xd} + Q_l}\right)^{7/12}\right], \tag{A13}$$

where

$$\eta_{xd}\left(l_0, C_n^2, D\right) = \frac{\eta_x}{1 + 0.40\eta_x\left(2 - \overline{\Theta}\right)/\left(\Omega_G + \Lambda\right)}, \tag{A14}$$

$$\frac{1}{\eta_x\left(l_0, C_n^2\right)} = \frac{0.38}{1 - 3.21\overline{\Theta} + 5.29\overline{\Theta}^2} + 0.47\sigma_1^2 Q_l^{1/6}\left[\frac{\left(\frac{1}{3} - \frac{1}{2}\overline{\Theta} + \frac{1}{5}\overline{\Theta}^2\right)}{1.22\overline{\Theta}}\right], \qquad \text{(A15)}$$

and $\overline{\Theta}$ and Λ are Gaussian beam parameters in the receiver plane.. For the on-axis portion of a beam wave, the part of $\sigma_{\ln x}^2$ that depends on L_0 is defined by[3]

$$\sigma_{\ln x}^2\left(l_0, L_0, C_n^2, D\right) = \sigma_{\ln x}^2\left(l_0, C_n^2, D\right)\Big|_{\eta_{xd} \to \eta_{xd0}}, \qquad \text{(A16)}$$

where

$$\eta_{xd0}\left(l_0, L_0, C_n^2, D\right) = \frac{\eta_{xd} Q_0}{\eta_{xd} + Q_0}. \qquad \text{(A17)}$$

The small-scale log-irradiance scintillation, $\sigma_{\ln y}^2$, for a beam wave (on axis) is defined by[3]

$$\sigma_{\ln y}\left(l_0, C_n^2, D\right) = \frac{1.27\sigma_1^2 \eta_y^{-5/6}}{1 + 0.40\eta_y / \left(\Omega_G + \Lambda\right)}, \qquad \text{(A18)}$$

where

$$\eta_y\left(l_0, C_n^2\right) = 3\left(\frac{\sigma_1^2}{\sigma_G^2}\right)^{6/5}\left[1 + 0.65\left(\sigma_G^2\right)^{6/5}\right], \tag{A19}$$

$$\sigma_G^2\left(l_0, C_n^2\right) = 3.86\sigma_1^2\left\{0.40\frac{\left[\left(1+2\Theta\right)^2 + \left(2\Lambda + 3/Q_l\right)^2\right]^{11/12}}{\left[\left(1+2\Theta\right)^2 + 4\Lambda^2\right]^{1/2}}\right.$$

$$\times\left[\sin\left(\frac{11}{6}\varphi_2 + \varphi_1\right) + \frac{2.61\sin\left(\frac{4}{3}\varphi_2 + \varphi_1\right)}{\left(\left(1+2\Theta\right)^2 Q_l^2 + \left(3 + 2\Lambda Q_l\right)^2\right)^{1/4}} - \frac{0.52\sin\left(\frac{5}{4}\varphi_2 + \varphi_1\right)}{\left(\left(1+2\Theta\right)^2 Q_l^2 + \left(3 + 2\Lambda Q_l\right)^2\right)^{7/24}}\right]$$

$$\left.\times\frac{13.40\Lambda}{Q_l^{11/6}\left[\left(1+2\Theta\right)^2 + 4\Lambda^2\right]} - \frac{11}{6}\left[\left(\frac{1 + 0.31\Lambda Q_l}{Q_l}\right)^{5/6} + \frac{1.10\left(1 + 0.31\Lambda Q_l\right)^{1/3}}{Q_l^{5/6}} - \frac{0.19\left(1 + 0.24\Lambda Q_l\right)^{1/4}}{Q_l^{5/6}}\right]\right\} \tag{A20}$$

$$\varphi_1 = \tan^{-1}\left(\frac{2\Lambda}{1+2\Theta}\right), \tag{A21}$$

$$\varphi_2\left(l_0\right) = \tan^{-1}\left[\frac{\left(1+2\Theta\right)Q_l}{3 + 2\Lambda Q_l}\right], \tag{A22}$$

where $\overline{\Theta}$ and Λ are Gaussian beam parameters in the receiver plane.

APPENDIX B
MATLAB PROGRAM USED TO COMPUTE CROSSWIND SPEED

```
% use the import data tool and create an array called data (there are 5
% header lines in the file).  Depending on when the data was taken, the
% PMTs were rearranged.  Before 6/22/06, the small aperture(PMT2) was on the
% bottom, after 6/22/06 the large aperture(PMT0) was on the bottom.



% THIS TAKES A 7-MINUTE DATA RUN WITH 's' SAMPLES/SEC AND CREATES TWO
% MATRICES, ONE FOR PMT1 DATA AND ONE FOR PMT2 DATA.  THE DATA IS
DIVIDED
% INTO A ONE-MINUTE SAMPLE PER COLUMN.



%!!!!!USER INPUTS!!!!!
SEP_DIST = .12;  %distance between centers of apertures in meters
s = 1000; % number of samples/sec


for i = 1:7
   n = 60*s*(i-1)+1;
   p = 60*s*i;
   pmt1(:,i)=data(n:p,3); %change number for diff PMT config
end


for i = 1:7
```

```
    n = 60*s*(i-1)+1;
    p = 60*s*i;
    pmt2(:,i)=data(n:p,2); %change number for diff PMT config
end

for i = 1:7
    pmt1_lin(:,i)=(100*10*10^-12).*(10.^((pmt1(:,i))./.2));
end

for i = 1:7
    pmt2_lin(:,i)=(100*10*10^-12).*(10.^((pmt2(:,i))./.2));
end

% COMPUTES THE CROSS-CORRELATION FROM PMT2 TO PMT1 (HOLDS PMT1
FIXED AND
% LAGS PMT2) FOR EACH OF THE 7 ONE-MINUTE DATA RUNS.  THEN OUTPUTS AN
% AVERAGED CROSSWIND SPEED VALUE.

% specify number of delay points
delay = [0:1:240];
for k = 1:7
```

```
    % create a zero-padded time shifted matrix
    XLAG = lagmatrix(pmt2_lin(:,k) , delay);       % Create the lagged matrix.
    % Change NaN in XLAG to zeroes
    TF = isnan(XLAG);
    [M,P] = size(XLAG);
    for i = 1:M
       for j = 1:P
          if TF(i,j) == 1
             XLAG(i,j) = 0;
          end
       end
    end
    % multiply the non-shifted column by each of the shifted ones
    [A,B] = size(delay);
    for i = 1:B
       PROD(:,i) = XLAG(:,i) .* pmt1_lin(:,k);
    end
    % sum each of the columns to create a cross-correlation value at each delay
    % time.  These sums produce a 1 x delay matrix.  These matrices are then
    % put in as separate rows, a new row for each one-minute data run.
    CORR(k,:) = sum(PROD);
end
clear XLAG TF PROD; % to save memory
```

```
% THIS IS THE SAME PROGRAM AS ABOVE, ONLY IT COMPUTES THE CROSS-
CORRELATION
% GOING IN THE OTHER DIRECTION, PMT1 TO PMT2



for k = 1:7
   % create a zero-padded time shifted matrix
   XLAG = lagmatrix(pmt1_lin(:,k) , delay);       % Create the lagged matrix.
   % Change NaN in XLAG to zeroes
   TF = isnan(XLAG);
   [M,P] = size(XLAG);
   for i = 1:M
      for j = 1:P
         if TF(i,j) == 1
            XLAG(i,j) = 0;
         end
      end
   end
   % multiply the non-shifted column by each of the shifted ones
   [A,B] = size(delay);
   for i = 1:B
```

```
    PROD(:,i) = XLAG(:,i) .* pmt2_lin(:,k);
  end
  % sum each of the columns to create a cross-correlation value at each delay
  % time.  These sums produce 1 x delay matrix.  These matrices are then
  % put in as separate rows, a new row for each one-minute data run.
  CORR1(k,:) = sum(PROD);
end
clear XLAG TF PROD; % to save memory


% IMPLEMENTS A MOVING AVERAGE FROM PMT2 TO PMT1 TO HELP SMOOTH
OUT THE DATA OVER EACH MINUTE.
% THE AVERAGE IS TAKEN USING HALF OF THE WINDOW SIZE ABOVE AND
BELOW
% THE PARTICULAR DATA POINT.


span = 15; % amount of data points to avg, needs to be an odd number
for i = 1:7
  CORR_AV_MOV(:,i) = smooth(CORR(i,:),span);
end
```

```
% IMPLEMENTS A MOVING AVERAGE FROM PMT1 TO PMT2 TO HELP SMOOTH
OUT THE DATA OVER EACH MINUTE.
% THE AVERAGE IS TAKEN USING HALF OF THE WINDOW SIZE ABOVE AND
BELOW
% THE PARTICULAR DATA POINT.



for i = 1:7
   CORR_AV_MOV1(:,i) = smooth(CORR1(i,:),span);
end



% CREATES A CORRELATION MATRIX WITH BOTH THE NEGATIVE AND POSITIVE
TIME
% DELAYS.  THIS IS USED TO PLOT THE COMPLETE CROSS-CORRLEATION FCN.



% each correlation matrix has a value for zero delay in the first row.  it
% needs to be removed from one of the matrices to avoid a duplicate.
for i = 1:7
   CORR_AV_MOV1_REV(:,i) = CORR_AV_MOV1(end:-1:1,i); % reverses order of matrix
end
CORR_AV_MOV1_FIX = CORR_AV_MOV1_REV(2:241,1:7); % removes zero delay
```

```
CORR_AV_MOV_TOT = [CORR_AV_MOV1_FIX',CORR_AV_MOV']; % concatanates the
two matrices
[A1,A2] = size(CORR_AV_MOV_TOT);
A3 = [-floor(A2/2):1:floor(A2/2)];
CORR_7MIN_AV_TOT = mean(CORR_AV_MOV_TOT); % 7-min average


% NORMALIZES THE TOTAL CORRELATION MATRIX AND THE 7-MINUTE
AVERAGE TOTAL
% CORRELATION MATRIX


for i = 1:7
   CORR_AV_MOV_TOT_NORM(i,:) = (CORR_AV_MOV_TOT(i,:) ./
max(CORR_AV_MOV_TOT(i,:)));
end

CORR_7MIN_AV_TOT_NORM = (CORR_7MIN_AV_TOT ./
max(CORR_7MIN_AV_TOT));


% ADDS TIME AND DATE STAMP FROM DATA FILE
```

```
day_time_start = textdata{6,1};
sprintf('Measurement began at %s', textdata{6,1}) %need to use {} b/c cells are used
[A,B] = size (data);
day_time_end = textdata{A,1};
sprintf('Measurement ended at %s', textdata{A,1})



% CREATES A MATRIX WITH THE TIME LAGS CORRESPONDING TO THE
MAXIMUM CORRELATION
% VALUES FROM EACH ONE-MINUTE DATA RUN AND PRINTS THE RESULTS TO
THE SCREEN.



for i = 1:7
   MAX(:,i) = find(CORR_AV_MOV_TOT(i,:) == max(CORR_AV_MOV_TOT(i,:)));
   TIME(:,i) = (-round(A2/2) + MAX(:,i)) ./ s;  % s represents number of samples per second
   WS(:,i) = SEP_DIST ./ TIME(:,i);
   sprintf('Cross wind speed for minute %d = %f m/s',i,WS(:,i))
end
```

```
% PLOTS 7-MINUTE AVERAGE PLOT AND SMOOTHED 1-MINUTE CORRELATION
PLOTS,
% WAITING FOR 'ENTER' KEY FROM USER AFTER EACH PLOT.

MAX_7MIN = find(CORR_7MIN_AV_TOT == max(CORR_7MIN_AV_TOT));
TIME_7MIN = (-floor(A2/2) + MAX_7MIN) ./ s;  % s represents number of samples per second
WS_7MIN = SEP_DIST / TIME_7MIN;
sprintf('Cross wind speed for 7 min average = %f m/s',WS_7MIN)

X_AXIS_TIME = A3 / s; % puts x-axis in seconds
plot(X_AXIS_TIME,CORR_7MIN_AV_TOT_NORM)
title(sprintf('July %s 2006',day_time_start(3:4)),'fontweight','bold','fontsize', 10)
xlabel('Delay Time (Seconds)','fontweight','bold','fontsize', 10)
ylabel('Normalized Cross-Correlation','fontweight','bold','fontsize', 10)
pause
for i = 1:7
   plot(X_AXIS_TIME,CORR_AV_MOV_TOT_NORM(i,:))
   title(day_time_start(1:10))
   xlabel('Delay Time (Seconds)')
   ylabel('Normalized Cross-Correlation')
   pause
end
```

LIST OF REFERENCES

[1] Al Naboulsi, M., Sizun, H., de Fornel, F., (2005). Propagation of optical and infrared waves in the atmosphere. URSI, XXVIII, F01P.7.

[2] Andrews, Larry, C., Phillips, Ronald, L. (2005). Laser Beam Propagation through Random Media 2nd Edition. Bellingham, WA: SPIE Press.

[3] Andrews, Larry, C., Phillips, Ronald, L., Hopen, Cynthia, Y. (2001). Theory of Scintillation: Plane Wave Model. In *Laser Beam Scintillation with Applications* (pp. 97-125). Bellingham, WA: SPIE Press.

[4] Hill, Reginald, J. (1983). Inner scale effect on the irradiance of light propagating in atmospheric turbulence. Proc: SPIE, 410, 67.

[5] Leon-Garcia, Alberto, (1994). Random Processes. In *Probability and Random Processes for Electrical Engineering* (pp. 337). Reading, MA: Addison-Wesley.

[6] Luvera, Giovanni "Optical Turbulence Measurements and Analysis", Masters Thesis, University of Central Florida, (1997).

[7] Scintec AG, *Scintec Download Service*. (2006, April 19). Retrieved August 18, 2006, from http://www.scintec.com/update/update.php?Abschicken=Continue

[8] Stromqvist Vetelino, Frida, Clare, Bradley, Corbett, Kerry, (2006). Characterizing the propagation path in moderate to strong optical turbulence. *Applied Optics IP*, 45, 3534-3543.

[9] Stromqvist Vetelino, Frida, Young, Cynthia, Andrews, Larry, C. (2005). Scintillation: theory vs. experiment. Infrared Technology and Applications Proc: SPIE, 5793, 166-177.